Detection and reconstruction of short-lived particles produced by neutrino interactions in emulsion

Uiterwijk, J.W.H.M.

Chapter 1

Neutrino masses and oscillations

The neutrino was introduced as a hypothetical particle in 1930 by Pauli to solve the energy crisis in nuclear β-decay. Because of its extremely small cross-section to interact with matter, experimental neutrino physics only started much later. The basic interaction was first described by Fermi's theory and later unified in the electro-weak theory of the standard model of elementary particles.

When anomalously low fluxes of solar and atmospheric neutrinos were measured, neutrino oscillations were presented as a possible explanation for the missing neutrinos. In the last two decades, the experiments searching for neutrino oscillations have become more sensitive, culminating in clear evidence for oscillation of atmospheric neutrinos in 1998. This was followed in 2001 to 2003 by confirmation of the solar-model predicted flux for ^{8}B neutrinos and determination of the oscillation parameters causing the solar-neutrino disappearance.

This chapter is mostly dedicated to the physics of neutrino oscillations. It will introduce several aspects of the physics involving neutrinos, namely: the historic discoveries of the neutrinos; neutrino masses and mixing, including a simplified theory of oscillation; the parameter space explored by the CHORUS experiment; and an overview of the current results of oscillation experiments. This chapter concludes with a brief discussion of the current knowledge about neutrino mixing and an outlook to the remaining questions to be answered in the future.

1.1 Neutrino history

In the beginning of the 20th century, there was a fundamental problem in physics: energy seemed not to be conserved in certain radioactive decays. The energy of electrons emitted in β-decays did not have a definite value but instead a continuous spectrum. In 1930, Wolfgang Pauli, in his famous letter to the 'radioactives', postulated that an unknown neutral particle was present inside the nucleus which escaped unobserved in β-decays, carrying away the missing energy and momentum [2]. In 1934, Enrico Fermi developed a comprehensive theory of radioactive decays [3] involving Pauli's hypothetical particle which he named in Italian the 'little neutron'. Henceforth, this has stayed the particle's name: the 'neutrino'. The symbol used for this particle is the greek letter ν.

1.1.1 The electron neutrino

Fermi's calculations showed that a neutrino interacts only very weakly (or equivalently very rarely) with matter. At the time, the neutrino–matter interaction cross-section was considered too small for the neutrino to be detected. It was only 23 years after its postulation by Pauli, that the first experiment to detect electron neutrinos was set up by Reines and Cowan [4]. At a nuclear reactor, a prolific source of $\overline{\nu}_{\mathrm{e}}$ from β-decays of the neutron-rich fission products, anti-neutrinos were detected via the inverse β-decay process:[1]

$$\overline{\nu}_{\mathrm{e}} + p \rightarrow e^{+} + n \quad .$$

The detector consisted of liquid scintillator and dissolved cadmium-chloride. The light produced by fast electrons in the liquid scintillator was detected by photo-multiplier tubes. A neutrino interaction was identified by the delayed coincidence of two pulses: the first one originating from the two gammas from the e^{+} annihilation; the second, required to arrive several microseconds later, being the signal from the neutron captured by a cadmium nucleus. Within a year the first signals of neutrinos were seen [5], followed by statistically stronger evidence in 1956 [6].

1.1.2 The muon neutrino

The muon, a heavier version of the electron, was first detected with cloud-chambers in cosmic-ray experiments around 1935 [7–11]. In its decay, $\mu \rightarrow e$, the emerging electron shows a continuous energy spectrum with similar polarization as in radioactive β-decay. Assuming that Fermi's theory could also describe muon decay, there had to be three particles in the final state. It was natural to assume that the two undetected particles were both neutrinos. One of these neutrinos was associated with the electron (now known as the ν_{e}). The absence of electro-magnetic decay of the muon, $\mu \rightarrow e + \gamma$ via the process shown in Figure 1.1, was an indication for the existence of a second neutrino species associated with the muon, nowadays indicated as ν_{μ}.

[1] The symbols 'p' and 'n' stand for the proton and neutron. The symbols 'd' and 'α' will be used for the deuteron and the helium-4 nucleus. Occasionally, when the focus is on isotope composition, the proton, deuteron and helium-4 nuclei will be given by the corresponding nuclear symbols: ^{1}H, ^{2}H and ^{4}He.

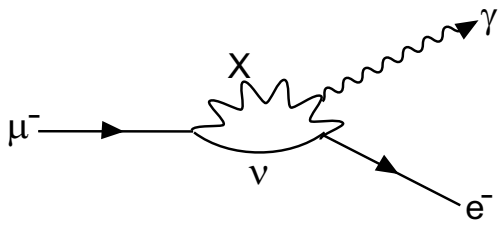

Figure 1.1: Unobserved possible Feynman diagram of $\mu \to e + \gamma$ as considered in the 1960s [12]. The interchanged heavy boson indicated by X is nowadays known as the $W^{\pm}$.

In 1962 at the Brookhaven national laboratory, using the first accelerator-generated neutrino beam ever built, muon neutrinos were identified as the neutral product in pion decays. It was known that the pion decayed to a muon and a neutrino, but the exact nature of this neutrino was unknown at that time. A 10-ton spark-chamber detector was placed behind a 17 m thick shield, made from recycled armour of scrapped battle ships. All particles produced by interactions of a 15 GeV proton beam in a beryllium target were stopped inside the shielding, only the neutrinos from pion decays could pass through it. If these neutrinos were the same as the neutrinos from nuclear β-decay, the experiment should have observed as much electrons as muons. Instead, the experiment observed several neutrino interactions in the detector, all of which were accompanied by a muon [13]. This result proved that the muon and electron were part of two separate families of leptons, each with their own neutrino. Instead of families, the terms generations or flavours[2] are also used.

1.1.3 The tau neutrino

After the discovery of the tau lepton in 1975 [14], it was assumed that also the τ had its associated neutrino, the ν_τ. Further indications came from the following arguments: the τ decay kinematics [15]; the number of light neutrino species measured to be 2.994 ± 0.012 [1] from the invisible Z^0 width [16]; the non-observation of ν_e or ν_μ induced τ production (see also section 2.1); the deduction from $\tau \to \rho$ decays that the ν_τ has spin 1/2 [17]; the measurement of the weak isospin of the τ^- with as result $T_3 = -1/2$ from neutral-current lepton-pair production ($Z^0 \to \ell^+ \ell^-$) at LEP [18] and the parity violation in the same process for polarized $e^+ e^-$ at SLC [19]. This last results implies that the τ is part of a weak-isospin doublet with a weak-isospin partner, the ν_τ.

It took until 2001 before the detection of a charged-current ν_τ interaction was made by the DONUT experiment at Fermilab [20]. This delay is due to the lack of abundant sources of ν_τ neutrinos. Only by placing a detector capable of identifying τ tracks behind a beam dump of a 800 GeV proton beam could four charged-current ν_τ interactions be identified. Inside the beam dump, only short-lived particles can decay before they re-interact. All other particles are absorbed or are swept out by the applied magnetic field. Behind the beam dump, the relative ν_τ flux is therefore enhanced. The ν_τ originate mostly from the decay $D_s^+ \to \tau^+ \nu_\tau$ or $D_s^- \to \tau^- \overline{\nu}_\tau$ (branching ratio of $[6.4 \pm 1.5]\,\%$) and the subsequent τ decay.

[2]Strictly speaking, flavour is used to indicate one of the six different quarks, one of the three different charged leptons or one of the three neutrinos.

The DONUT experiment had a similar setup as the CHORUS experiment (described in Chapter 2) with emulsion and electronic detectors. To analyze the DONUT emulsion data, the FKEN laboratory in Nagoya had to develop new, much faster, scanning hardware and new event reconstruction techniques than was foreseen for the CHORUS emulsion analysis. The new event reconstruction, called net-scan, can reconstruct the τ track as well as the primary and decay vertices. These new developments, explained in section 2.10.3, have later been adopted to do a much more extensive analysis of CHORUS emulsion data and made the charm-quark study in Chapter 5 possible.

1.2 The standard model

A complete discussion of the standard model of elementary particles and interactions (SM) can be found in many of the standard text-books on particle physics, for example Ref. 21. This section presents a brief overview of the particles and parameters of the SM.

1.2.1 Particles and forces

In Figure 1.2, the twelve fermions in the SM are shown: six quarks and six leptons organized in three families. There are thirteen bosons transmitting the three elementary forces included in the SM: the Higgs gives mass to particles; the electro-magnetic interaction is transmitted by the photon; the strong interaction is transmitted by eight coloured gluons; and the weak interaction is transmitted by the $W^{\pm}$ and Z^0 bosons in charged-current and neutral-current weak interactions, respectively. The fourth elementary force, gravity, is not (yet) described by the SM.

All the forces are symmetric under the parity (coordinate inversal) P, the charge-conjugation C (particle↔anti-particle interchange) and the time-reversal T operators, except for the weak interaction. The $W^{\pm}$ couples only to the left-handed chirality states of the fermions (right-handed for anti-particles), while the Z^0 couples differently to left and right-handed fermions. The weak interaction therefore violates P symmetry. Furthermore, the charged-current weak interaction is particular as it is the only interaction that transforms the fermion. The maximum violation of P symmetry by the weak interaction, proposed by Lee and Yang [22], was first demonstrated in the β-decay of spin-polarized ^{60}Co [23] and later in the kinematics of the pion and muon decays [24,25]. More recently, it was discovered that also the combined CP symmetry, long thought to be conserved in weak decays, was violated in K^0 decays [26]. The $W^{\pm}$ has a different coupling with each quark. The charged-current weak interaction changes one quark into another, violating both quark-type and family-number conservation laws. These laws are obeyed separately by all other interactions, including the neutral-current weak interaction. Strangely enough, the charged-current does obey family conservation laws in the lepton sector.

The quarks in Figure 1.2 are named: up 'u', down 'd', strange 's', charm 'c', bottom 'b' and top 't'. The charged-current preferably couples the quarks within a family ($u \leftrightarrow d$, $s \leftrightarrow c$, $b \leftrightarrow t$), known as a Cabibbo-enhanced transformations. The transformation of quarks between the first two families ($u \leftrightarrow s$, $d \leftrightarrow c$) are known as Cabibbo-suppressed transformations. Cabibbo discovered (before the charm quark was found) that the suppression in the decay rate of strange-quark containing particles, could be described by a single parameter, now known as the Cabibbo angle θ_C [27]. It turned out that the

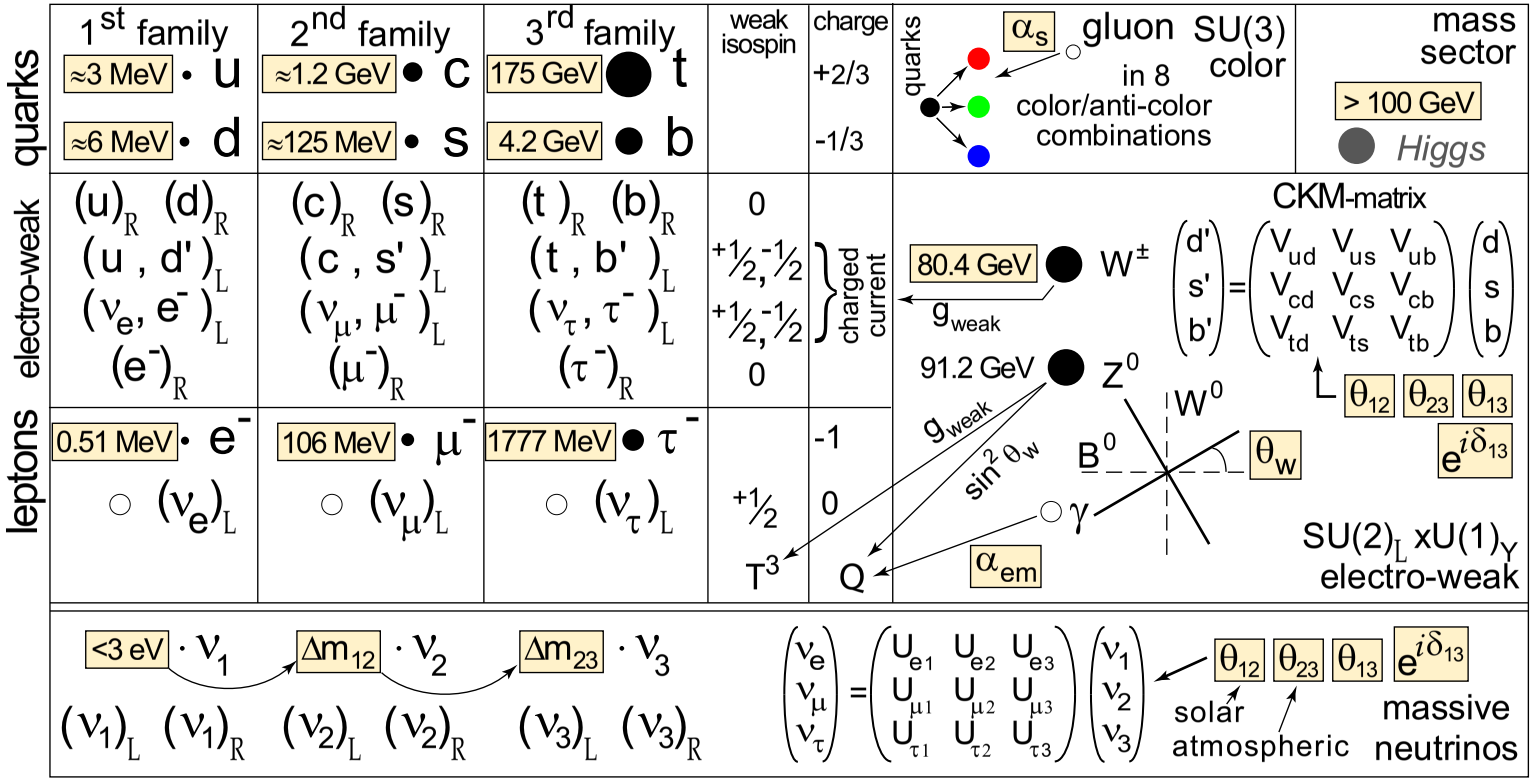

Figure 1.2: Schematic representation of the standard model of elementary particles and forces. The fermions from the three families are shown on the left. The four bosons responsible for the three basic interactions are shown on the right and their coupling with the fermions is indicated by the arrows. Open circles indicate massless particles, all other masses are parameters of the standard model. The parameters which can only be determined from measurements are shown inside the gray boxes. The Higgs particle is drawn in gray, because it has not yet been detected and its mass is only known indirectly. The extension of the standard model required by massive neutrinos is indicated below the line at the bottom.

coupling between the quarks in the first two families could be described by a rotation matrix with θ_C as the rotation angle. The $W^{\pm}$ couples (in the approximation with only two-families) to the linear combination of $|d\rangle \cos\theta_C + |s\rangle \sin\theta_C$, with $\sin^2(\theta_C) \approx 0.05$. In general, the quark couplings by the charged-current interaction can be described by a 3×3 unitary matrix, known as the Cabibbo, Kobayashi, Maskawa (CKM) matrix [28]. The CKM matrix is parametrized by a complex phase for CP-violation and three mixing angles, one of which is θ_C. The CKM matrix describes how the quark eigenstates of the strong and electro-magnetic interaction connect to the charged-current weak-interaction eigenstates. The CKM matrix, shown on the right-hand side of Figure 1.2, is by convention applied to the lower half of the quark doublets.

Interestingly, the charm quark was proposed on symmetry and theoretical grounds, before its discovery in the J/Ψ resonance [29, 30]. A fourth quark was necessary to explain the anomalously slow decay of the $K^{\pm}$ [31, 32]. In hind-sight, charmed mesons had already been seen earlier in emulsion events [33]. In a similar fashion, the third family was postulated before any quark or lepton of the third generation was discovered. Instead, the motivation was a desire to explain CP violation within the Cabibbo scheme. This requires a complex number in the rotation matrix, but with only two families such a term can always be eliminated by a suitable redefinition of the quark phases.

1.2.2 Parameters and constants

The SM has been very successful in predicting the outcome of many experiments and allows the calculation (in theory) of many high-energy particle interactions. However, the SM contains quite a few parameters (constants in the Lagrangian) which have to be measured by experiment and are an input to the SM. These parameters are indicated by the gray boxes in Figure 1.2 and include the masses of the particles and the coupling constants of the forces. The goal of the grand-unified theory (GUT) is to derive these parameters from basic principles and include the gravitional force. The unification of the electro-magnetic and weak interaction demonstrated the relation between several parameters which were considered independent before. The Weinberg weak-mixing angle relates the weak and electro-magnetic coupling constants and the W and Z mass. One could argue that the particular structure of the families (also its number) and interactions, which follows as a consequence of the $\mathrm{U}(1) \otimes \mathrm{SU}(2)_L \otimes \mathrm{SU}(3)$ group structure of the SM, introduces another concept to be explained by theory. For example, the electron charge is by definition -1 because the electro-magnetic coupling strength α contains the basic electric charge e. However, there might be a deeper correlation between the fractional charge of the quarks and the family structure (3 quark colours with the electron and neutrino in a single SU(5) multiplet with total charge zero).

1.2.3 Neutrinos

In the SM, neutrinos appear as the weak-isospin partners of the left-handed charged leptons ℓ (e, μ or τ). The coupling to the $W^{\pm}$ bosons is via the weak charged-current:

$$J_{\mu}^{CC} = \overline{\psi}_{\nu_\ell} \gamma_\mu \frac{1}{2}(1 - \gamma^5)\psi_\ell \quad , \tag{1.1}$$

where γ_μ are the Pauli-Dirac spin matrices and ψ are the 4-component spinor wave-functions of the particles. The coupling of ψ_{ν_ℓ} to ψ_ℓ in equation (1.1) indicates that the

neutrino flavour is uniquely identified by the production of the corresponding charged lepton ℓ in charged-current interactions. The maximum parity violation is expressed by the term $(1-\gamma^5)$ which projects out the left-handed chirality component of the ψ_ℓ wave-function.

The weak neutral-current coupling of the Z^0 boson to the fermions has the form

$$J_\mu^{NC} = \overline{\psi}_f \gamma_\mu \frac{1}{2}(c_V^f - c_A^f \gamma^5)\psi_f \quad , \tag{1.2}$$

where c_V and c_A are the vector and axial-vector couplings. For fermions, they are given by $c_V^f = T_f^3 - 2\,Q_f \sin^2(\theta_{\rm W})$ and $c_A^f = T_f^3$. Here Q_f is the electric charge of the fermion f and T_f^3 is the third component of the fermion's weak isospin. The neutral-current reflects the mixing between the weak and electro-magnetic forces via the Weinberg or electro-weak mixing angle $\theta_{\rm W}$. For neutrinos $Q = 0$ and $T^3 = 1/2$ and equation (1.2) becomes

$$J_\mu^{NC} = \overline{\psi}_\nu \gamma_\mu \frac{1}{4}(1-\gamma^5)\psi_\nu \quad ,$$

which has the same structure as equation (1.1), describing a coupling with the left-handed helicity states only. The right-handed leptons are $SU(2)_L$ weak-isospin singlets with $T^3 = 0$ and couple only via the $2\,Q_f$ term in the vector coupling c_V^f in equation (1.2). A right-handed neutrino has both $Q = 0$ and $T^3 = 0$ and therefore does not couple via either the electro-magnetic or the charged-current and neutral-current weak interactions. As all leptons are colour-less, a right-handed neutrino also does not interact via the strong force. Right-handed neutrinos are therefore completely sterile in the SM and the question of their existence is meaningless if they are massless as well.

1.2.4 Neutrino–matter interactions and cross-sections

To understand how experiments detect neutrinos, it is important to consider the interactions of neutrinos and anti-neutrinos with matter and how the cross-sections and kinematics of these reactions depend on energy. In this section, the basic principles will be outlined. As described above, neutrinos or anti-neutrinos can interact with matter either via the charged-current or the neutral-current weak interaction.

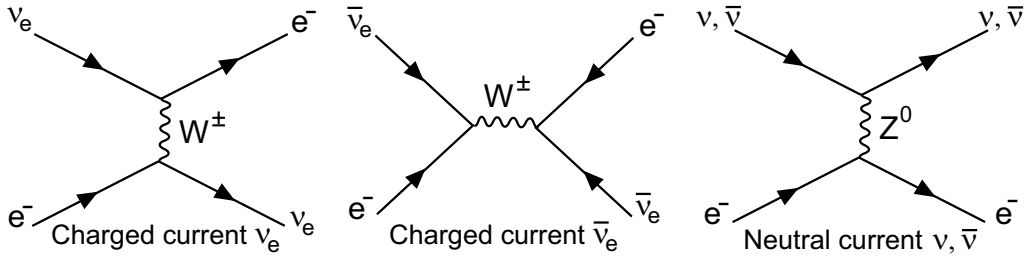

Figure 1.3: First order Feynman diagrams for scattering of $\nu_{\rm e}$, ν_μ and ν_τ and the anti-neutrinos on electrons. There are two diagrams for $\nu_{\rm e}$ and $\overline{\nu}_{\rm e}$ scattering because both the charged-current and neutral-current contribute. For ν_μ and ν_τ and their anti-particles only the neutral-current is possible, which is the same for all neutrino and anti-neutrino types.

Neutrino–electron scattering

The theoretically best understood reaction is between (anti-)neutrinos and electrons, because the electron can be considered as an elementary and free particle. The first order Feynman diagrams are shown in Figure 1.3. For ν_e and $\overline{\nu}_e$, the neutral-current and charged-current amplitudes interfere, while for ν_μ, $\overline{\nu}_\mu$, ν_τ, and $\overline{\nu}_\tau$ only the neutral-current contributes. The cross-section is therefore about a factor 6 larger for electron (anti-)neutrinos than for muon or tau (anti) neutrinos.

Furthermore there is a difference between neutrinos and anti-neutrinos due to the maximum parity violation of the weak interaction. For neutrinos the interaction has zero total angular momentum and the scattering angle is isotropic. For anti-neutrinos, the total angular momentum is one and, as can be easily seen from helicity arguments, backward scattering is suppressed. For anti-neutrinos the angular distribution is given by $1 - \cos\theta$, with θ the angle between the direction of the neutrino before and after the scattering. Consequently, the cross-section for anti-neutrino scattering is about a factor three smaller than for neutrino scattering. Figure 1.4 shows the cross-sections for neutrino–electron and anti-neutrino–electron scattering as function of the Weinberg weak-mixing angle θ_W [34]. A determination of the cross-sections for the different neutrinos was actually used to determine θ_W.

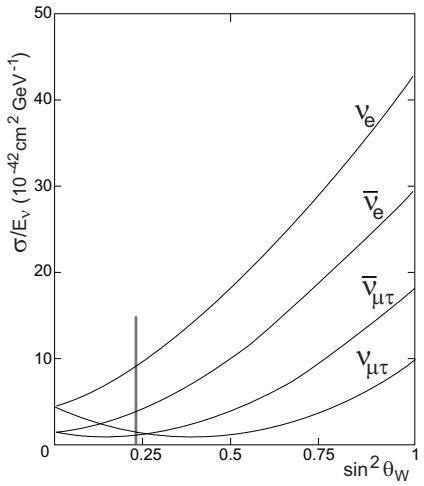

Figure 1.4: Standard model calculated cross-sections for neutrino and anti-neutrino scattering on electrons as function of the weak-mixing angle θ_W. The vertical line at $\sin^2\theta_W = 0.23$ indicates the actual value of θ_W.

Neutral–current interactions

The neutral-current scattering of (anti-)neutrinos with nucleons or nuclei is similar to electro-magnetic electron–nucleon interactions, but with much smaller coupling strength. Instead of a photon, a (virtual) Z^0 boson is exchanged. Like the electro-magnetic interaction, neutral-current reactions have no intrinsic energy threshold. For high-energy neutrino experiments, one is mostly concerned with deep-inelastic scattering, where the momentum and energy transfer is so high that the Z^0 couples to a quark inside a nucleon and produces a shower of secondary particles. However, the SNO experiment (discussed in section 1.6.2) uses low-energy neutral-current interactions, where the Z^0 dissociates a deuterium nucleus with a threshold energy of 2.224 MeV.

Charged–current interactions

For charged-current (anti-)neutrino interactions with nuclei, the interactions can be categorized more or less by the energy and momentum transferred by the (virtual) $W^{\pm}$ boson. First of all, charged-current interactions have a threshold energy because of the produced lepton in the $\nu_\ell \rightarrow W^{\pm} + \ell$ reaction. Typically, ν_μ (ν_τ) neutrinos below 106 MeV (1.8 GeV) do not interact via charged-current reactions.

At energies less than several MeV, the $W^{\pm}$ interacts with the nucleus or nucleon as a whole and causes proton↔neutron transitions. This process — the inverse of radioactive β-decay — is used in low-energy solar-neutrino experiments. At medium energy ($E \approx 1\,\text{GeV}$), the $W^{\pm}$ knocks out the converted proton or neutron from the nucleus. These processes are called quasi-elastic interactions (QE). In an experiment, QE events are characterized by a single lepton track with possibly a short, low-energy, proton track. The cross-section for QE reactions as function of the neutrino energy E_ν is shown in Figure 1.5a [34]. It rises up to $0.9 \cdot 10^{-5}$ nb at 20 GeV above which it stays approximately constant due to the nucleon form-factor.

At energies above 1 GeV, deep-inelastic scattering (DIS) becomes dominant. In deep-inelastic scattering the $W^{\pm}$ couples to a quark inside a nucleon. The struck quark then changes flavour according to the CKM matrix couplings and is knocked out of the nucleon. The struck quark and the remains of the nucleon lead to a particle shower inside a detector. The flavour-changing interaction leads to a significant production of strange and charmed quarks. The cross-section for DIS scattering of neutrinos and anti-neutrinos is shown in Figure 1.5b [34].

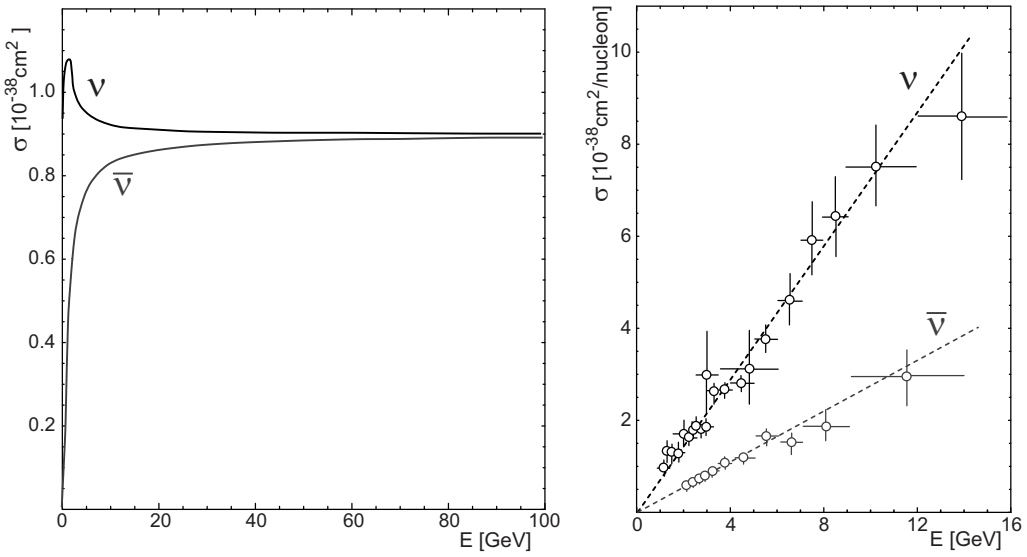

(a) (b)

Figure 1.5: Cross-sections for (anti-)neutrino↔nucleon scattering for (a) quasi-elastic and (b) deep-inelastic scattering as a function of the neutrino energy.

1.2.5 Beyond the standard model

In 1998, the Super-Kamiokande experiment (see section 1.4.4) published convincing evidence for neutrino oscillation. As oscillations require neutrinos to have mass, the neutrino masses need to be added to the SM. Masses and oscillations of neutrinos can be accommodated in the SM Lagrangian, but they add at least another 7 parameters, as indicated at the bottom of Figure 1.2. Furthermore, right-handed neutrinos exists as well because helicity is not a conserved quantity for particles with a non-zero mass. The question is then what this right-handed neutrino state corresponds to. Depending on the exact form of the mass term, the right-handed neutrino state can correspond to the anti-neutrino or to an independent neutrino state. In the first case, the neutrino is a Majorana particle, in the second case it is a Dirac particle. The difference between these two cases will be briefly discussed in section 1.8.

1.3 Neutrino masses and oscillation

Neutrino oscillation was first proposed by B. Pontecorvo in 1957 [35,36]. In this section, neutrino-oscillation phenomenology is discussed within the context of the simplest case of two-flavour mixing. First, an overview of the current limits from direct neutrino-mass measurements is given.

1.3.1 Direct mass measurements

When attempting to directly measure neutrino masses, it is always assumed that the mass eigenstates ν_1, ν_2 and ν_3 are composed mainly of one weak-interaction eigenstates ν_e, ν_μ and ν_τ respectively. Below, mass limits are quoted for these weak eigenstates since they correspond to the neutrino species investigated in the experiments.

Limit on m_{ν_e}

The square of the electron neutrino mass $m^2_{\nu_e}$ is measured in tritium β-decay experiments by fitting the shape of the electron spectrum near the endpoint. The current best limits come from the Mainz and Troitsk experiments [37,38]. Because the flux of electrons near the end-point of the tritium decay spectrum diminishes very rapidly, a high-intensity tritium source is needed. At the same time, though, no material can be introduced between the source and the spectrometer. To get enough statistics for a meaningful determination of the mass, these experiments require an extremely accurate spectrometer with very large acceptance. The PDG review gives a combined upper limit on the electron neutrino mass of $m_{\nu_e} < 3\,\mathrm{eV}$ at 95 % confidence level [1].

Limit on m_{ν_μ}

The ν_μ mass is constrained by measuring the muon momentum in pion decays:

$$\pi^+ \rightarrow \mu^+ + \nu_\mu \quad .$$

Combined with the best knowledge of the muon and pion masses, this yields the present best limit of $m_{\nu_\mu} < 190\,\mathrm{keV}$ at 90 % confidence level [1,39].

Limit on m_{ν_τ}

Upper limits on m_{ν_τ} are obtained by studying the kinematics of hadronic τ-decays. The analysis involves the calculation of the hadronic invariant mass and fitting the energy spectrum of the hadronic system [40]. The best result comes from the ALEPH collaboration quoting an upper limit for the tau neutrino mass $m_{\nu_\tau} < 18.2\,\mathrm{MeV}$ at 95 % confidence level [41].

Mass differences

For the moment it seems difficult to explore absolute mass values significantly below the current limits performing direct measurements. The upper limits on the mass differences that can be established from the above results practically coincide with the actual mass limits. This happens because the neutrino mass limits follow the pattern of the corresponding leptons: $m_e \ll m_\mu \ll m_\tau$. As is shown in the following sections, neutrino oscillations provide the means to probe mass differences which may be smaller than the lowest neutrino mass limit. Mass differences determined in neutrino oscillation experiments therefore establish upper limits on the absolute mass of the heavier neutrinos very close to the upper limit on the mass of the lightest neutrino.

1.3.2 Neutrino oscillation

If neutrinos have mass, the weak eigenstates ν_e, ν_μ, and ν_τ do not necessarily coincide with the mass eigenstates ν_1, ν_2, and ν_3 and lepton flavour is no longer a conserved property of the neutrino. Hence flavour transitions may take place in vacuum. The original proposition of neutrino oscillation considers oscillation between $\nu \leftrightarrow \overline{\nu}$ (the muon and tau neutrino had not yet been discovered). The same idea applies, though, to flavour oscillations [42].

To illustrate the effect of mixing in the propagation of a massive neutrino, only the simplest case assuming two flavours and two mass eigenstates is considered here. Despite its simplicity, this is a basic assumption underlying the data analysis carried out by most oscillation experiments. The results of such an analysis can be presented in a single plot of a two-dimensional oscillation parameter space. In the more realistic situation with three flavours and three masses, the two-flavour analysis result still provides a good description in the limiting case where the third flavour consists only of the third mass eigenstate or in the case that the mass differences are very different such that the phase in equations (1.8) and (1.9) for one mass difference is small with respect to the other.

Vacuum oscillation

The flavour eigenstates ν_ℓ and $\nu_{\ell'}$ can be described as a superposition of the mass eigenstates ν_1 and ν_2 according to a 2×2 unitary mixing matrix:

$$\begin{pmatrix} \nu_\ell \\ \nu_{\ell'} \end{pmatrix} = \begin{pmatrix} \cos\theta & \sin\theta \\ -\sin\theta & \cos\theta \end{pmatrix} \begin{pmatrix} \nu_1 \\ \nu_2 \end{pmatrix} \quad ,$$

where θ is known as the mixing angle. At production (for example in a weak decay) neutrinos are created in a definite flavour eigenstate ν_ℓ. Assuming that a neutrino is

produced in a weak decay as ν_ℓ with momentum p, its wave-function at $t = 0$ is:

$$|\nu_\ell\rangle = \cos(\theta)\,|\nu_1\rangle + \sin(\theta)\,|\nu_2\rangle \quad . \tag{1.3}$$

Working with the natural system of units, where $c = \hbar = 1$, the evolution of the wave function in time will be

$$|\nu_\ell(t)\rangle = \cos(\theta)\,e^{-iE_1 t}\,|\nu_1\rangle + \sin(\theta)\,e^{-iE_2 t}\,|\nu_2\rangle \quad . \tag{1.4}$$

Here

$$E_i = \sqrt{p^2 + m_i^2} \approx p + \frac{m_i^2}{2p} \quad , \tag{1.5}$$

assuming that the neutrino is highly relativistic such that $p^2 \gg m_i^2$. From equation (1.5), it follows that

$$E_1 - E_2 \approx \frac{\Delta m^2}{2p} \approx \frac{\Delta m^2}{2E} \quad , \tag{1.6}$$

with $\Delta m^2 = m_1^2 - m_2^2$. The probability that the neutrino will still be found as ν_ℓ after traveling some distance $L = ct$ is then given by:

$$P_{\nu_\ell \to \nu_\ell}(L) = |\langle \nu_\ell(0) | \nu_\ell(t) \rangle|^2 \quad . \tag{1.7}$$

Substituting the expressions from equations (1.3), (1.4), and (1.5) in equation (1.7) and using (1.6), one obtains

$$P_{\nu_\ell \to \nu_\ell}(L) \approx 1 - \sin^2(2\theta)\,\sin^2\left(\frac{\Delta m^2 L}{4E}\right) \quad . \tag{1.8}$$

Similarly, the transition probability $P_{\nu_\ell \to \nu_{\ell'}}$, which is the probability for the neutrino to interact as $\nu_{\ell'}$ rather than ν_ℓ, is given by:

$$P_{\nu_\ell \to \nu_{\ell'}}(L) = \sin^2(2\theta)\,\sin^2\left(\frac{\Delta m^2 L}{4E}\right) \quad . \tag{1.9}$$

The quantity $P_{\nu_\ell \to \nu_{\ell'}}$ given in equation (1.9) is known as the oscillation probability. From the above equations, one can define the oscillation length

$$L_{osc} \equiv 4\pi \frac{E}{\Delta m^2} \quad , \tag{1.10}$$

which is the travel distance needed to go from ν_ℓ to a maximally mixed state and back to ν_ℓ. It is customary to express Δm^2 in eV^2, L in km and E in GeV. The oscillation probability and oscillation length are then given respectively by

$$P_{\nu_\ell \to \nu_{\ell'}}(L) = \sin^2(2\theta)\,\sin^2\left(1.267 \frac{\Delta m^2 L}{E}\right) \tag{1.11}$$

and

$$L_{osc} = \frac{\pi E}{1.267 \Delta m^2} \quad . \tag{1.12}$$

In the case that $L_{osc} < \Delta L$, with ΔL the range of detected flight lengths, or if there is a wide spectrum of neutrino energies in the source, the L/E ratio can take on many values at the detector. In this case the oscillation pattern is lost, hence the probabilities in equations (1.8) and (1.9) become equal to their time averaged values

$$P_{\nu_\ell \to \nu_\ell} = 1 - \frac{1}{2}\sin^2(2\theta) \tag{1.13}$$

and

$$P_{\nu_\ell \to \nu_{\ell'}} = \frac{1}{2}\sin^2(2\theta) \quad , \tag{1.14}$$

respectively. This happens in most accelerator generated neutrino beams (section 2.2) where the distance between the source and the experiment is of the same order as the length of the decay tunnel. It is also the case for atmospheric and (most) solar neutrinos (see section 1.4) which have both wide energy spectra and a large spread in flight lengths.

Matter enhanced oscillation

When neutrinos undergo elastic scattering with charged leptons, they interact differently according to the flavour of the charged lepton. The elastic-scattering process

$$\nu_{\ell'} + \ell^- \to \nu_{\ell'} + \ell^-$$

takes place only via a neutral-current interaction if $\ell' \neq \ell$, while if $\ell' = \ell$ the transition amplitudes of the neutral and charged-current interfere. When neutrinos propagate in matter, they undergo elastic interactions with electrons. For large regions, this can lead to coherent effects in the oscillation. The elastic forward scattering can be described in terms of a potential energy

$$V = V_Z + V_W \quad ,$$

where V_Z and V_W are the potential energies due to Z^0 and $W^\pm$ exchange respectively. Since there are no muons or taus in ordinary matter, the V_W term exists only for electron neutrinos. Assuming that electrons in matter are at rest with constant electron density N_e, the potential V_W is given by:

$$V_W = \sqrt{2} G_F N_e \quad ,$$

where G_F is the Fermi weak coupling constant.

Wolfenstein, Mikheyev, and Smirnov [43, 44] pointed out that the effect of coherent forward scattering can change the oscillation pattern of neutrinos traveling through matter. For such a mixing, with given Δm^2 and $\sin^2(2\theta)$ in vacuum, the observed oscillation pattern in matter could be described by the effective values

$$\Delta m^2_{\text{eff}} = \Delta m^2 \sqrt{\left(a - \cos(2\theta)\right)^2 + \sin^2(2\theta)} \tag{1.15}$$

and

$$\sin^2(2\theta_{\text{eff}}) = \frac{\sin^2(2\theta)}{\left(\cos(2\theta) - a\right)^2 + \sin^2(2\theta)} \quad , \tag{1.16}$$

where

$$a = 2\sqrt{2} G_F N_e \frac{E}{\Delta m^2}$$

In the limit that $a \to \cos(2\theta)$, one gets as effective oscillation parameters from equation (1.15) and (1.16):

$$\lim_{a \to \cos(2\theta)} \Delta m^2_{\text{eff}} = \Delta m^2 \left| \sin(2\theta) \right| \tag{1.17}$$

and

$$\lim_{a \to \cos(2\theta)} \sin^2(2\theta_{\text{eff}}) = 1 \quad , \tag{1.18}$$

describing an effective maximal mixing in matter. This resonance behaviour, the so-called MSW effect, may take place if N_e has the appropriate value. In this case the observed Δm^2_{eff} is smaller than the vacuum Δm^2.

1.3.3 Oscillation detection methods

Neutrinos created in a flavour eigenstate will oscillate to other eigenstates during propagation. Such oscillation can in principle be detected in two ways, appearance and disappearance.

Appearance experiments

An experiment which detects a neutrino flavour absent in the source is known as an appearance experiment. The sensitivity of these experiments depends on the number of positive events with respect to the expected background. The most convincing oscillation signal is to unequivocally detect a neutrino flavour from its charged-current reaction in a channel where there is no background.

Because of the energy-threshold in charged-current reactions, these experiments are usually only sensitive to oscillation with high Δm^2 unless they use very long baselines. On the other hand, an appearance experiment can detect small mixing angles if it can acquire a large event sample. The last requirement usually implies a short baseline to create a high neutrino flux and therefore reduces further the sensitivity to low Δm^2.

Disappearance experiments

In a disappearance experiment, one tries to detect a deficit in the neutrino flux with respect to the theoretical flux for a given source. Most experiments with natural neutrino sources are disappearance experiments, because the neutrino energy is below the threshold for muon or tau production. One exception is the SNO experiment's neutral-current measurement, discussed in section 1.6.2.

These experiments are only sensitive to large mixing angles, because a small deficit will be drowned in the statistical and theoretical uncertainties of the neutrino flux. On the other hand, they can detect very small Δm^2 by tuning the neutrino energy and baseline such that $L/E \approx 1$. The most convincing evidence for neutrino oscillation in a disappearance experiment is to measure the characteristic sinusoidal disappearance of the neutrino flux as function of L/E.

Parameter extraction

In general, for any oscillation experiment, the only observable is the number of neutrino interactions. Depending on the experiment, these can be categorized by the neutrino flavour (for charged-current interactions) and, in some cases, the energy. In some circumstances, the incoming neutrino direction can be reconstructed. In such a case, an analysis as function of L/E becomes possible, for example for high-energy atmospheric neutrinos.

From the number of interactions for ν_ℓ and $\nu_{\ell'}$ (the last only for appearance experiments), constraints can be placed on the range of allowed values [45] of the oscillation probabilities $P_{\nu_\ell \to \nu_\ell}$ (disappearance) and $P_{\nu_\ell \to \nu_{\ell'}}$ (appearance), usually as function of energy. The interpretation of this experimental value in terms of theoretical parameters, such as neutrino masses and mixing angles, depends on the underlying theoretical model and the experimental constants, in particular the neutrino-energy spectrum and the flight-length distribution. Most experiments restrict the analysis to the simplest case of two-flavour mixing, which has two mixing parameters as given in equation (1.11), $\sin^2(2\theta)$ and Δm^2. The experimental results can then be presented as excluded or favoured regions in the $\sin^2(2\theta)$, Δm^2 plane in a simple 2-D contour plot, see for example Figure 1.11.

1.4 Neutrino oscillation hints

In this section, some of the hints that something was going on with neutrinos will be discussed. The recent experimental results will be discussed in section 1.7 in which a summary of the current neutrino-oscillation results is presented.

1.4.1 Cosmology

The contributions from different particles and forces to the total energy density of the universe determines its evolution in time. These contributions are usually expressed as fractions $\Omega_i \equiv \rho_i/\rho_c$ of the critical energy density $\rho_c = 3H_0^2/(8\pi G_\mathrm{N})$ required for a flat universe. At the critical density, the expansion rate, given by the Hubble constant H_0, is exactly balanced by the gravitational attraction of which the strength is given by Newton's constant G_N. Figure 1.6 gives a schematic view of the components of the total energy density.

The requirement for dark matter in Figure 1.6 is based, among others, on the discrepancy between the amount of luminous matter and its measured velocities in spiral galaxies. The rotational velocities of stars around a galaxy's center are too high to keep the galaxy together based on the gravitational influence of the visible matter. Assuming that the structure of galaxies is long-lived, more matter must be present inside the orbits of the stars to keep the galaxy together. Similar measurements on the relative motion of galaxies inside galaxy clusters or super-clusters indicate the presence of vast amounts of non-visible matter. However, dark matter has been an ever shifting target over the last 30 years. Different quantities of dark-matter have been proposed with yet again different fractions of hot (relativistic and therefore exerting a positive pressure) and cold (non-relativistic) matter. The cosmological constant causes the expansion to speed up and was reintroduced because of supernova type-I measurements.

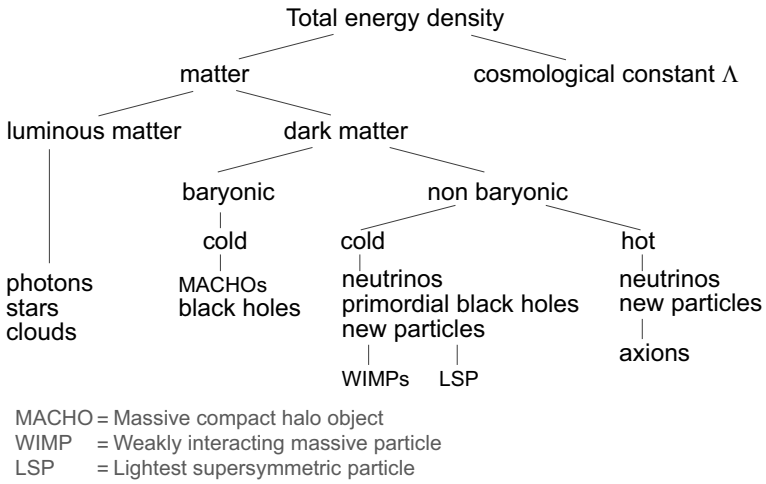

Figure 1.6: Schematic view of the total energy density of the universe, showing the different contributions to the energy density.

The amount of dark-matter required to explain the velocities of stars far exceeds the visible baryonic matter in the universe. From all proposed contributions to the dark-matter in Figure 1.6, only the neutrino is known to exist.[3] Neutrinos are highly abundant in the universe with about 100 neutrinos of each flavour per cubic-centimeter. For a long time, massive neutrinos were considered a very good candidate for dark matter. Nowadays, the current results on neutrino masses from oscillation experiments and upper limits on the total neutrino mass from the microwave background measurements exclude that neutrinos are a substantial part of the dark matter.

Only in recent years, with the accurate measurements of the cosmic microwave background anisotropy by the WMAP satellite, have the relative contributions of matter and other-fields to the total density of the universe settled down a bit. The current WMAP results give a cold dark-matter contribution to the energy content of the universe of 23 % plus 4 % normal (baryonic) matter of which again only about $1/10^{\text{th}}$ is in visible (luminous) matter [51]. The total neutrino mass is now limited to less than 0.68 eV. For more details, the reader is referred to reviews in the literature, like Refs. 1, 52, 53.

1.4.2 Solar neutrinos

When it became clear in the beginning of the 20^{th} century that the age of the solar system should be measured in billions of years, it was realized that gravitational contraction could not have sustained the sun's energy output for this time. When it also became known that the sun is mainly composed of hydrogen and helium (discovered in solar spectral lines), it was sir Arthur Eddington who proposed that nuclear fusion could be the sun's energy source. It took until 1938 before a theory of the nuclear reactions within the sun was developed by Bethe and Chritchfield [54, 55]. The sun's main energy source is provided by the fusion of four protons plus two electrons into one tightly-bound helium-4 nucleus and two electron neutrinos, liberating 26.73 MeV in energy.

[3] Some MACHOs [46, 47] have been observed from micro-lensing effects, but far too few to contribute significantly to the baryonic dark matter [48–50].

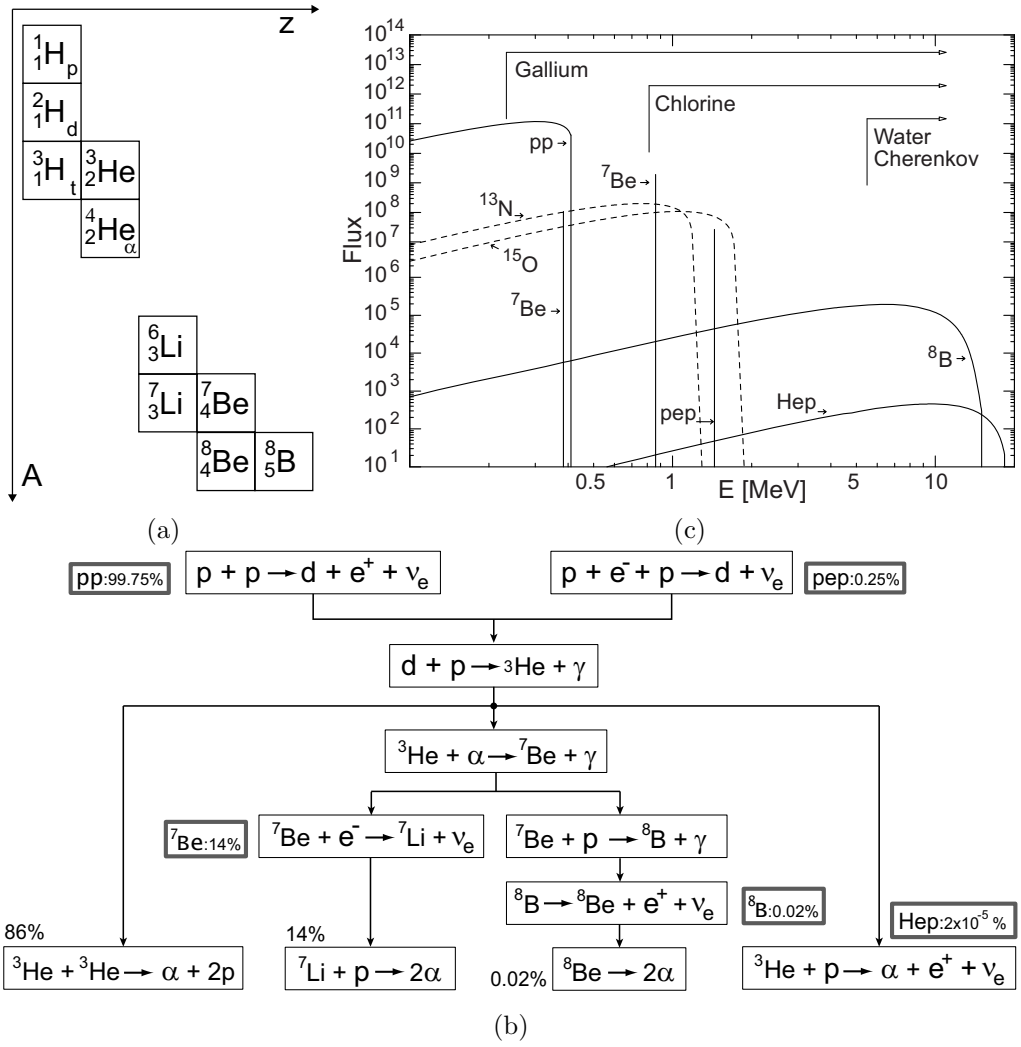

Figure 1.7: (a) The different isotopes involved in the solar fusion reactions. (b) Schematic diagram of the different pathways for the same overall fusion reaction: $4p \rightarrow {}^4_2\mathrm{He} + 2e^+ + 2\nu_\mathrm{e}$. The relative abundance for the ν_e producing reactions are also given. (c) The ν_e spectrum.

The fusion actually proceeds via four different paths with several intermediate steps, as illustrated in the diagram of Figure 1.7b. The relative strength of the paths depends strongly on the exact energy levels of the nuclei and on the temperature and density in the interior of the sun. These dependencies lead to uncertainties in the overall ν_e spectrum. This spectrum, shown in Figure 1.7c, consists of line-spectra from electron-capture reactions and continuous spectra from $p \rightarrow n$ reactions. A less important contribution is due to fusion reactions catalyzed by ^{12}C, known as the CNO cycle. In the standard solar model (SSM), the neutrino flux is calculated from the equation of state. The SSM has been verified by checking its sound-velocity predictions with measurements from helio-seismology which agree to within 0.1 % RMS [56, 57].

As 99.75 % of the fusion paths start with the pp reaction, its ν_e flux is strongly correlated with the total energy production in the sun, which in turn is directly connected with the observed total luminosity. Therefore, the pp ν_e flux should be proportional to the sun's luminosity. However, the diffusion time for photons and energy from the sun's core to its surface is about $1.7 \cdot 10^5$ and $3 \cdot 10^7$ years, respectively [58, 59], while the neutrinos escape immediately. Since the sun is currently in a very stable phase of its stellar evolution, the equilibrium between fusion energy and luminosity is not influenced by the time-lag between photons and neutrinos.

As can be seen in Figure 1.7c, most of the solar neutrinos (99.9 %) have an energy below 1 MeV. As a consequence, these solar neutrinos can only be detected with a reaction with a threshold lower than 1 MeV. One process sensitive to such low energy ν_e is the inverse β-decay reaction on some nucleus X: ${}^{A}_{Z}\mathrm{X} + \nu_e \rightarrow {}^{A}_{Z+1}\mathrm{Y} + e^-$. The energy threshold for this reaction is lowered by the mass difference between neutron and proton and the difference in nuclear binding energies. Experiments for solar-neutrino detection based on the ${}_{Z}\mathrm{X} \rightarrow {}_{Z+1}\mathrm{Y}$ reaction require a large amount of the target nucleus X and therefore its (relative) isotope abundance on earth must be high. The two nuclei involved, X and Y, must also fulfill other criteria. First, the mass-difference $M(\mathrm{Y}) + 511\,\mathrm{keV}/c^2 - M(\mathrm{X})$ must be small or negative to have an energy threshold below the typical energy of the solar neutrinos. Second, in order to count the number of neutrino interactions, the created atoms Y must be counted and therefore the elements must be separable by some means. Since the number of target atoms must be very large, direct separation by, for example, a mass spectrometer is not possible. Another physical or chemical difference is required for the separation. If counting relies on the radioactive decay of nucleus Y, its half-life must be long enough so that its concentration can grow in the target before decaying and short enough so that its decays can be measured after extraction. Experiments based on this technique are known as radio-chemical experiments.

The first experiment to measure solar neutrinos, Homestake, was started by Davis Jr. in the 1960s using the reaction ${}^{37}\mathrm{Cl} + \nu_e \rightarrow {}^{37}\mathrm{Ar} + e^-$ [60, 61]. This reaction has a threshold energy of 814 keV and is therefore only sensitive to the ${}^{7}\mathrm{Be}$ and ${}^{8}\mathrm{B}$ neutrinos, as indicated in Figure 1.7c. The chlorine was contained in cleaning fluid ($\mathrm{C_2Cl_4}$) from which the noble gas argon can be extracted by flushing with helium. The isotope ${}^{37}\mathrm{Cl}$ has a natural relative abundance of about 24 % and ${}^{37}\mathrm{Ar}$ decays by electron-capture with a half-life of 34.8 days.

A reaction with a lower threshold (233 keV) is between gallium and germanium: ${}^{71}\mathrm{Ga} + \nu_e \rightarrow {}^{71}\mathrm{Ge} + e^-$ [62]. As germanium is normally a solid, they are actually used as liquid metallic gallium or dissolved $\mathrm{GaCl_3}$ and gaseous $\mathrm{GeCl_4}$. The isotope ${}^{71}\mathrm{Ga}$ has a natural relative abundance of about 40 % and ${}^{71}\mathrm{Ge}$ decays by electron-capture with a half-life of 11.4 days. Even though the pp flux is dominant, the above reaction is only caused for about 55 % by pp. The ${}^{7}\mathrm{Be}$ and ${}^{8}\mathrm{B}$ neutrinos contribute for approximately 27 % and 10 %, respectively, because of their higher energy. Two experiments, Gallex and SAGE, started measuring this reaction in 1990. Gallex used 30 tons of gallium in solution of $\mathrm{GaCl_3}$, while SAGE used from 30 to 60 tons of liquid metallic gallium.

The results of radio-chemical experiments are usually expressed in solar-neutrino units (SNU) which corresponds to one neutrino capture per 10^{36} target atoms per second. The predictions for the chlorine and gallium experiment from one solar model are given in Table 1.1. For 30 ton of material, the quoted interaction rates correspond at most to some tens of created Y atoms after exposure for two to three half-lives.

reaction	Standard Solar Model flux [$cm^{-2}s^{-1}$]	^{37}Cl [SNU]	^{71}Ga [SNU]
pp	$5.94 \cdot 10^{10}$	-	69.6
^{7}Be	$4.80 \cdot 10^{9}$	1.15	34.4
pep	$1.39 \cdot 10^{8}$	0.2	2.8
^{8}B	$5.15 \cdot 10^{6}$	5.9	12.4
hep	$2.10 \cdot 10^{3}$	0.0	0.0
CNO	$1.14 \cdot 10^{9}$	0.5	9.8
Total		$7.7^{+1.2}_{-1.0}$	129^{+8}_{-6}

Table 1.1: Fluxes and interaction rates for the chlorine and gallium experiments from the solar model of Ref. 63.

The Homestake experiment has been running almost continuously from 1970 until 1994. From the beginning its results were lower than expected from solar models. This low solar-neutrino flux has since been known as the "solar-neutrino problem". Homestake measured a flux of below 3 SNU [64, 65], which is about $1/3^{\text{th}}$ of the expected flux. The difficulty of this type of experiment is illustrated by the fact that in the 24 years that Homestake has run, only an estimated 2200 argon atoms were produced in the tank which contained $2 \cdot 10^{30}$ chlorine atoms!

Both Gallex and SAGE needed more than a year to reduce an unexpected background from long-lived ^{68}Ge (half-life 271 days) created from the gallium by cosmic-rays when it was still at the surface. In the initial five runs, SAGE detected almost no signal [66] and set an upper limit of 79 SNU (90 % confidence level). Later results of SAGE were in better accordance with the Gallex measurement of $83 \pm 19(\text{stat}) \pm 8(\text{sys})$ SNU [67], which was the first detection of pp neutrinos from the sun.

The upgraded Kamiokande nucleon decay experiment, Kamiokande-II (KamII), started measuring solar neutrinos in 1986. In contrast to the radio-chemical experiments, KamII could measure the interactions in real-time and measure the direction of the incoming neutrinos. However, because of the energy threshold of 7.5 MeV, it was only sensitive to the high-energy component of the solar spectrum, namely the ^{8}B neutrinos. Detection was done using the neutrino–election scattering reaction in which the electron direction is correlated with the incoming neutrino direction. The KamII detection technique was later used by the, much larger, follow-up experiment, Super-Kamiokande. A detailed description can be found in section 1.6.1. In the KamII measurement [68], the correlation of the signal's direction with the position of the sun proved the existence of solar neutrinos (see also Figure 1.18). KamII measured a ratio for the ^{8}B flux of $[46 \pm 5(\text{stat}) \pm 6(\text{sys})]$ % with respect to the solar model of Ref. 69.

The results from all the solar-neutrino experiments could be reconciled if neutrino oscillation is responsible for the disappearance of solar neutrinos. Because of the high density of the sun, the MSW effect could effectively lead to maximum mixing which explained the low rates for Homestake and KamII. Time variation measurements (day versus night for MSW effects in the earth or seasonal for baseline variation) by Homestake and KamII and energy-dependence measurements by KamII further excluded certain regions in the oscillation parameter space [70]. Four regions in the Δm^2, $\sin^2(2\theta)$ plane could explain all the data. In three of these the MSW effect is important and one is due to pure vacuum oscillation [71, 72].

1.4.3 Atmospheric neutrinos

Atmospheric neutrinos are generated by the interaction of cosmic rays with the earth's atmosphere. Cosmic rays were discovered in the beginning of the last century. Electrically charged objects lose their charge even though the air surrounding them is an insulator, so something must be ionizing the air. First thought to be natural radioactivity, it was Hess who showed in 1912 that the charge leakage increases with altitude and is therefore due to something arriving from space [73]. The cosmic rays detected at the earth's surface are actually the remainders (mostly muons) of showers generated when high-energy primary particles, mostly protons and helium nuclei, strike the top of the atmosphere. Most of the secondary particles in the shower are pions which either reinteract or decay before reaching the earth's surface. Typical cosmic-ray showers start at an altitude between 25 km and 20 km. Because of the low atmospheric density, most of the low-energy ($E < 10\,\mathrm{GeV}$) $\pi^{\pm}$ ($c\tau = 7.8\,\mathrm{m}$) and $K^{\pm}$ ($c\tau = 3.7\,\mathrm{m}$) mesons produced in the showers decay before interacting:

$$\begin{array}{llll} \pi^+ \to \mu^+ + \nu_\mu & , & \pi^- \to \mu^- + \overline{\nu}_\mu & (\text{braching ratio } 99.99\,\%)\ , \\ K^+ \to \mu^+ + \nu_\mu & , & K^- \to \mu^- + \overline{\nu}_\mu & (\text{braching ratio } 63.51\,\%)\ . \end{array} \tag{1.19}$$

Most of the low-energy muons ($c\tau = 659\,\mathrm{m}$) also decay before reaching the ground:

$$\begin{array}{l} \mu^+ \to e^+ + \nu_\mathrm{e} + \overline{\nu}_\mu \\ \mu^- \to e^- + \overline{\nu}_\mathrm{e} + \nu_\mu \end{array} \quad (\text{braching ratio } 100\,\%)\ . \tag{1.20}$$

As the neutrinos hardly interact with the earth's matter, neutrinos will be incident on a detector from all directions. Atmospheric neutrinos therefore have flight lengths from about 15 km from directly overhead to 13000 km from straight below.

The observed energy spectrum of incoming primary particles reaches up to $10^{20}\,\mathrm{eV}$. Above $5 \cdot 10^{19}\,\mathrm{eV}$, the GZK cut-off due to interactions with the cosmic microwave background comes into play [74,75]. The incoming flux of primary particles can be considered isotropic, but at energies below several GeV the earth's magnetic field influences the primary flux. Consequently, atmospheric neutrinos cover a wide range of energies and the flux is isotropic above a few GeV, but not below. Furthermore, the sun's solar wind also influences the primary flux and leads to fluctuations coupled to the eleven year sunspot cycle.

Early Monte-Carlo calculations, predicted the flux of each neutrino species with an error of about 20 %. However, many of the uncertainties cancel in the flux ratio

$$r = \frac{\phi(\nu_\mu) + \phi(\overline{\nu}_\mu)}{\phi(\nu_\mathrm{e}) + \phi(\overline{\nu}_\mathrm{e})}\ , \tag{1.21}$$

which at low energies should equal 2, according to equations (1.19) and (1.20). The ratio r is predicted with an error of about 5 %. The value of r and its energy dependence from recent calculations is plotted in Figure 1.8 [101]. At higher energies ($E > 3\,\mathrm{GeV}$) the probability of muon decay is reduced and r rises.

Most oscillation searches using atmospheric neutrinos are performed by looking for possible deviations of the measured flux ratio compared to the Monte-Carlo. This is usually expressed as the double ratio

$$R_\mathrm{atm} = \frac{r_\mathrm{data}}{r_\mathrm{Monte-Carlo}}\ , \tag{1.22}$$

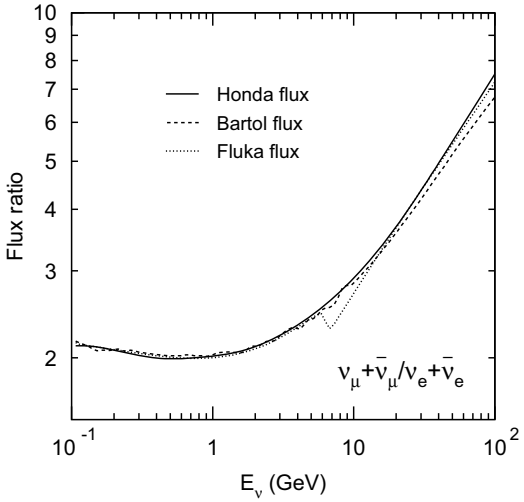

Figure 1.8: The flux ratio of $\nu_\mu + \overline{\nu}_\mu$ to $\nu_\mathrm{e} + \overline{\nu}_\mathrm{e}$ versus neutrino energy averaged over all zenith and azimuth angles. Solid, dashed and dotted lines show the predictions by three different flux models.

In this, the detection efficiency for each neutrino species in a particular experiment is taken into account. The low flux of the atmospheric neutrinos makes these measurements difficult as they require a large target mass and very good rejection of the backgrounds, like the much higher atmospheric-muon flux due to the decays given in equation (1.19). The measured values of R_atm in the early 1990s did not give a clear picture, the water-Cherenkov experiments yielded values below 1, while the iron calorimeters showed no difference from the expectations.

Early atmospheric-flux results

The first measurement came from the Kamioka Nucleon Decay Experiment (Kamiokande) in Japan, which measured a value of R_atm of 0.6 [76]. Later measurements by the water-Cherenkov detectors, all at energies below 1.5 GeV, also yielded values of R_atm less than 1 [77–80]. The detection and analysis of atmospheric-neutrino interactions in the water-Cherenkov detectors is explained in sections 1.6.1 and 1.7.1. The 1992 result of the Kamiokande-II experiment is based on 310 fully-contained, single-ring, quasi-elastic, neutrino interactions, classified as 159 electron-like (e-like) and 151 muon-like (μ-like) events [77]. Taking into account the detection efficiencies for ν_e and ν_μ interactions, the measured ratio was

$$R_\mathrm{atm} = 0.60^{+0.07}_{-0.06}(\mathrm{stat}) \pm 0.05(\mathrm{sys}) \quad ,$$

which is more than 4σ different from one. Similarly, the 1992 IMB result [80], is based on 610 events and gave $R_\mathrm{atm} = 0.70$ and 2.6σ below one. Looking at the rate of ν_e and ν_μ interactions individually, the experiments indicated that the measured deficit was mostly due to a low $\nu_\mu + \overline{\nu}_\mu$ rate. Both experiments performed a cross-check on the muon identification by tagging stopped muons from the $\mu \to e$ decay, with essentially identical results. Both experiments did not see any dependence on either momentum, $100\,\mathrm{MeV}/c < p < 1500\,\mathrm{MeV}/c$, or on neutrino flight length (zenith angle). At the same time, the iron-calorimeters, NUSEX and FREJUS, measured values of R_atm compatible with 1 [81–84]. The first measurement for higher-energy muons events ($E > 1\,\mathrm{GeV}$) by IMB, based on upward-going muons, showed also no difference from the Monte-Carlo expectation [85].

1.4.4 The 1998 Super-Kamiokande result

In 1998, the Super-Kamiokande experiment, described in detail in section 1.6, published its high-statistics measurements of atmospheric neutrinos [86]. Not only did these results confirm the earlier low value of R_{atm} and extended it to higher energies, but they also showed a clear dependence of the ν_μ flux on zenith angle and energy. These dependencies, shown in Figure 1.9, are fitted very well with the expectation of $\nu_\mu \to \nu_\tau$ oscillation using $\sin^2(2\theta) = 1$ and $\Delta m^2 = 2.1 \cdot 10^{-3}\,\mathrm{eV}^2$ [86].

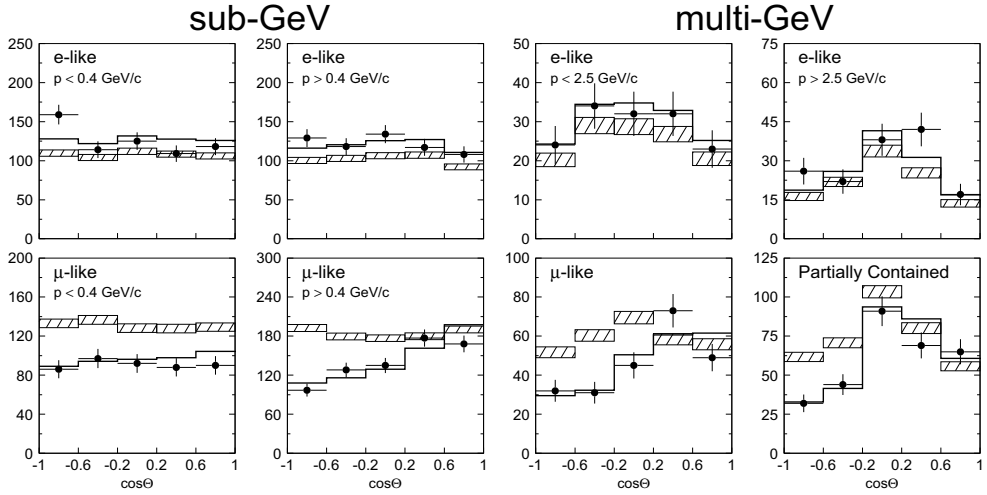

Figure 1.9: Zenith angle distribution for e-like and μ-like atmospheric-neutrino events in Super-Kamiokande. The partially contained events are mostly high-energy ν_μ interactions, where the muon leaves the inner detector. The points show the data, the dashed boxes the Monte-Carlo expectation without oscillation and the solid lines the best-fit expectation for $\nu_\mu \to \nu_\tau$ oscillation with $\sin^2(2\theta) = 1$ and $\Delta m^2 = 2.1 \cdot 10^{-3}\,\mathrm{eV}^2$.

At lepton momenta below $0.4\,\mathrm{GeV}/c$, there is basically no correlation between the lepton and neutrino direction, therefore there is no zenith angle dependence and only an overall ν_μ disappearance can been seen. The zenith angle is connected to the neutrino flight length L, with $L \approx 13\,\mathrm{km}$ for $\cos\theta = 1$ and $L \approx 13000\,\mathrm{km}$ for $\cos\theta = -1$. With the fitted Δm^2, the oscillation length is $L_{osc} \approx 1200\,E/\mathrm{GeV\,km}$. For $p < 0.4\,\mathrm{GeV}/c$ and maximum mixing, one then expects to see 75 % of the expected ν_μ flux, the average of 50 % fully-oscillated and 100 % non-oscillated fluxes, as is indeed the case for the μ-like, $p < 0.4\,\mathrm{GeV}/c$ events. At higher energies, where there is good correlation between lepton and neutrino direction, one can clearly see the ν_μ disappearance at long flight lengths, reaching 50 % of the expected flux for $\cos\theta = -1$. There is no disappearance of ν_e, nor is there any clear sign of ν_e appearance where ν_μ disappears. Therefore, no oscillation is expected from ν_μ to ν_e (also excluded by reactor and solar-neutrino results). Thus the oscillation is expected to be from ν_μ to ν_τ.

The oscillation hypothesis can be better analysed looking at the L/E dependence. The measurement of e-like and μ-like events as function of L/E is depicted in Figure 1.10 [86]. Here it is clear that e-like events are unaffected, while μ-like events show the characteristic fall-off with L/E, going to an average of 1/2 when L/E is much larger than the oscillation length.

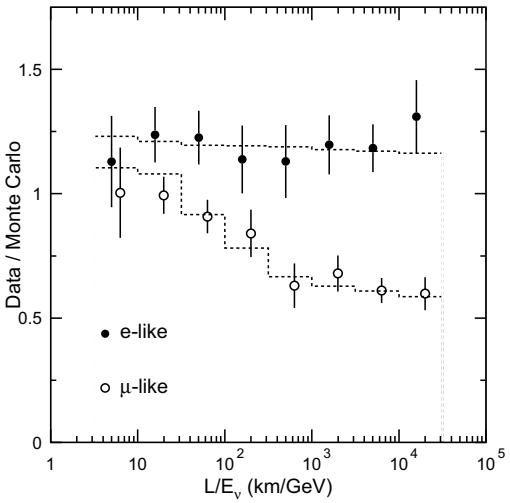

Figure 1.10: Super-Kamiokande events plotted as function of L/E show the characteristic disappearance of μ-like events with larger L/E, while the e-like events are unaffected. The dashed lines show the best $\nu_\mu \to \nu_\tau$ oscillation fit to the data.

Since 1998, the Super-Kamiokande results have been confirmed by continuing and new measurements. An overview of the current neutrino-oscillation experiments and results is discussed in the sections 1.6 and 1.7.

1.5 The CHORUS oscillation search

The lower than expected neutrino fluxes from natural sources, led to several searches for neutrino oscillations in artificial sources, like nuclear reactors and accelerator beams. These sources have the advantage that their neutrino fluxes are more controllable and better understood, thus removing the uncertainties from modeling either the solar nuclear processes or the atmospheric cosmic-ray showers.

1.5.1 Motivation

Many of the earlier accelerator experiments were not primarily designed to study neutrino oscillation. A dedicated experiment could substantially expand the excluded parameter region or actually detect neutrino oscillation. Accelerator neutrino beams, described in Chapter 2, consist primarily of muon neutrinos with a few percent electron neutrinos and are quasi-free of tau neutrinos. It is therefore natural to try to detect the oscillation of a muon neutrino into a tau neutrino as this gives a basically background free result.

Around 1990, a proposal to search for $\nu_\mu \to \nu_\tau$ oscillation with a new experiment, called CHORUS, was proposed. The detection technique used is discussed in Chapter 2. At the time, the expectation was that the mixing angles for neutrino oscillation were small, in accordance with quark mixing (section 1.2). Low mixing angles imply that the weak eigenstates are almost identical to the mass eigenstates. It was also expected that the mass eigenstates would have the same hierarchy as the leptons and quarks, such that $m_{\nu_e} \ll m_{\nu_\mu} \ll m_{\nu_\tau}$. With a limit for $m_{\nu_e} \lesssim 10\,\text{eV}$ at that time, cosmic-relic neutrinos were a good candidate to explain dark-matter if the heaviest mass eigenstate would be around 15 eV [87].

CHORUS was approved to take data in 1994 and 1995, later extended for two more years. A second complementary experiment, NOMAD, using a different detection technique based on kinematical cuts, was approved as well [88].

1.5.2 Excluded parameter space

In the simplest analysis of the CHORUS data, the main experimental observables are the total number of neutrino interactions N_{total} and how many of these are ν_τ interactions N_{ν_τ}. The CHORUS experiment did not detect any ν_τ in a sample of $N_{\text{total}} = 5 \cdot 10^5$. The expected background in this sample is about one event. The region CHORUS can then exclude for $\nu_\mu \to \nu_\tau$ oscillation is shown in Figure 1.11 together with an earlier result of NOMAD. The final exclusion limits for oscillation from the NOMAD experiment can be found in Ref. 89.

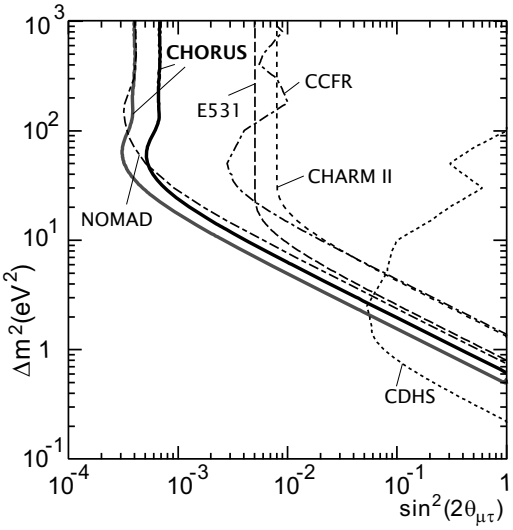

Figure 1.11: Exclusion plot for the result of the CHORUS experiment [90] and results from NOMAD and earlier experiments. The two curves for CHORUS use a different statistical analysis. The left-most curve is based on the same statistical approach as used by NOMAD. Using the same approach makes it possible to compare the individual results.

The shape of the excluded region can be understood by examining how the oscillation parameters influence the detected number of events. The oscillation probability, given by equation (1.11) for the two-flavour case, is proportional to:

$$P_{\nu_\mu \to \nu_\tau} \propto \frac{N_{\nu_\tau}}{N_{\text{total}}} \cdot \varepsilon(\nu_\mu, \nu_\tau) \quad ,$$

where $\varepsilon(\nu_\mu, \nu_\tau)$ accounts for all differences in cross-sections and detection efficiencies between ν_μ and ν_τ interactions. The excluded region for N_{ν_τ} compatible with the expected background is limited by two asymptotes in the log-log contour plot. The vertical asymptote at high Δm^2 determines the sensitivity to the mixing angle. Its position is inversely proportional to N_{total}. The other asymptote determines the minimum Δm^2 value at maximum mixing. This asymptote moves upward linearly towards smaller mixing angles, because the minimum Δm^2 as function of $\sin^2(2\theta)$ is proportional to

$$\Delta m^2_{\text{min}} \propto \left\langle \frac{E}{L} \right\rangle \frac{1}{\sin^2(2\theta) \cdot \sqrt{N_{\text{total}}}} \quad . \tag{1.23}$$

The behaviour of the exclusion limit at the bending point depends on the distribution of neutrino energies and flight lengths in the beam. From equation (1.23), it is clear that the minimum detectable Δm^2 for CHORUS only decreases inversely proportional to $\sqrt{N_{\text{total}}}$. To detect smaller Δm^2, one has to move to lower energies or longer baseline without letting N_{total} decrease as well.

1.6 Current neutrino experiments

The current evidence for neutrino oscillations come from basically three experiments which have similar experimental setups: in Japan, Super-Kamiokande (SuperK) and the Kamioka Liquid-scintillator Anti-Neutrino Detector (KamLAND); in Canada, the Sudbury Neutrino Observatory (SNO). Below, the general characteristics of these experiments are described first, before discussing each detector's particularities. The combined oscillation results are given in section 1.7.

The detectors consist of an inner and outer detector consisting of a large volume of liquid monitored by photo-multiplier tubes (PMTs). The inner detector serves as neutrino target, while the outer detector acts as an active veto. Accurate timing on the PMTs allows to reconstruct the interaction vertex and the direction of a produced muon or electron shower. A set of PMTs facing the outer detector detects charged particles entering the detector. Schematic drawings of the detectors are given in Figure 1.12. The experimental setups are described in detail in Ref. 94 for SuperK, Ref. 93 for SNO and Ref. 91 for KamLAND.

As the product of flux and cross-section is typically very low, these experiments are huge. The mass of the inner detectors is, respectively, 32000, 1000, and 1000 tons for SuperK, SNO and KamLAND. Even with these massive targets, the interaction rate is only of the order of a few events per day. Therefore, extreme care must be taken to suppress background from radioactive decays of radon, uranium and thorium contamination. Hence, these experiments require extreme purity of the filling liquids. Special care needs also to be taken to reduce radioactivity from the materials used in the supporting structures, the PMTs and the read-out electronics. Both SuperK and SNO require the signal to have a (visible) energy above 5 MeV, because the background from radioactivity is mostly at energies below 5 MeV. The detectors are placed deep underground to reduce the background from atmospheric muons. The outer detectors shield the detection volume from neutrons and environmental radioactivity. They also act as a veto for incoming muons or charged particles from neutrino interactions in the surrounding rock.

Muon-induced spallation of oxygen nuclei (and carbon for KamLAND) is found to be one of the main backgrounds. These spallation products have anomalous neutron/proton ratios and therefore all kinds of decay modes, like β and inverse β-decay, gamma emission, and proton or neutron emission. For the neutron sensitive detectors, SNO and KamLAND, the neutron emitters are particularly problematic. However, these nuclei have typically very short half-lives and therefore decay close to their production point. As a passing muon can be detected and its path reconstructed, the background from muon-induced spallation can be reduced by removing events in time (a few millisecond) and spatial (a few meter for neutrons) coincidence with a passing muon track.

The main difference between the detectors is the liquid used in the inner detector, water in SuperK, heavy water in SNO, and liquid scintillator in KamLAND. Therefore, the different detectors are sensitive to different processes. SuperK and SNO use Cherenkov radiation to detect a neutrino interaction, while KamLAND uses scintillation light and can measure the total energy deposited in the inner detector better than the other two experiments.

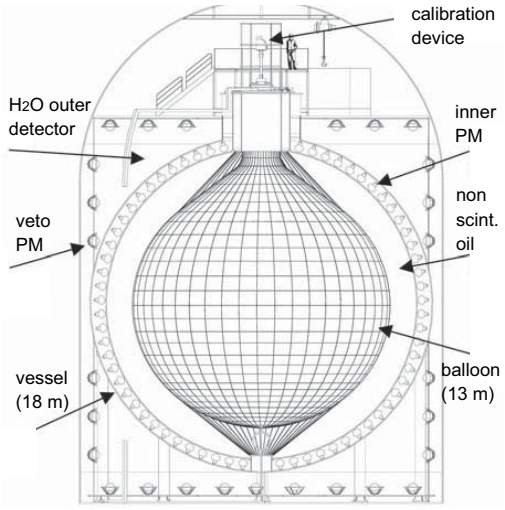

KamLAND [92]

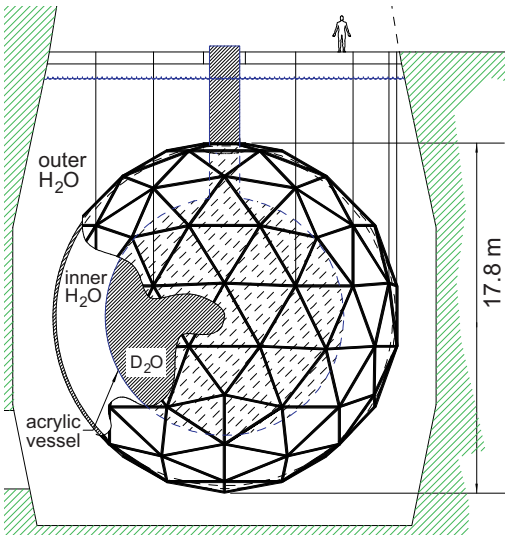

SNO [93]

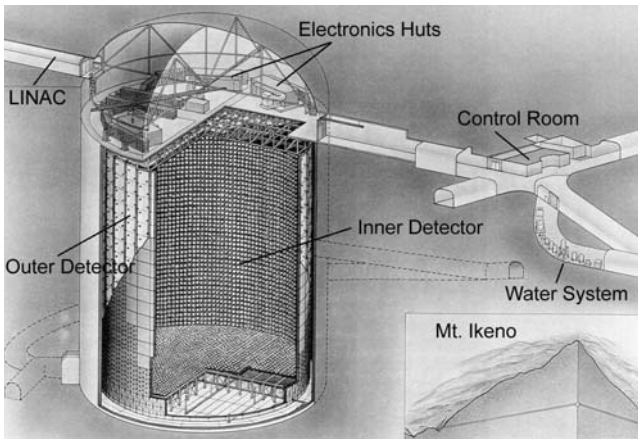

Super-Kamiokande [94]

Figure 1.12: The experimental setups of SuperK, SNO and KamLAND characterized by an inner and outer detector monitored by large photo-multiplier tubes.

1.6.1 Super-Kamiokande

The superK detector is a 39.3 m diameter, 42 m high barrel of water. Around the inner detector, 33.8 m in diameter and 36.2 m heigh, a steel construction houses the PMTs pointing both inward and outward. The superK detector is sensitive to both solar and atmospheric neutrinos. It can identify the Cherenkov light produced by muons and electrons.

Atmospheric-neutrino detection

Atmospheric neutrinos from 10 MeV to 10 GeV can be detected via quasi-elastic (QE) and deep-inelastic charged-current reactions (DIS). In a QE interaction, the emerging lepton will generate Cherenkov radiation which is detected as a single ring of hit PMTs. The hit pattern depends on whether the lepton is a muon or an electron. For a muon, this ring

has sharp boundaries. For an electron or positron, on the other hand, the Cherenkov light is generated by electrons and positrons inside a quickly developing electro-magnetic shower and the hit pattern is generally more fuzzy. This difference is clearly visible, as shown in Figure 1.13 [101]. A likelihood analysis of the hit pattern is used to classify single-ring events as electron-like (e-like) or muon-like (μ-like).

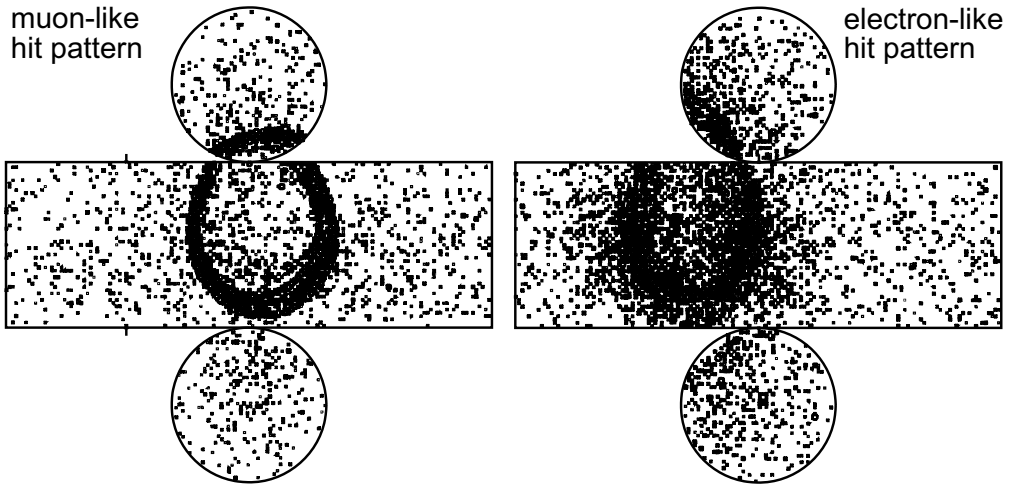

Figure 1.13: Different single-ring hit patterns in SuperK, resulting from Cherenkov light from a single muon on the left and from an electron on the right. Each point represents a hit PMT.

Deep-inelastic interactions produce multiple rings from the different charged particles. However, a classification into electron and muon events can still be made based on the brightest ring (highest number of hits), normally associated with the leading lepton. The separation into ν_e and ν_μ events is however not so good as for single ring events because the corresponding likelihood distributions overlap. As a result, the e-like classification contains only 50 % real ν_e charged-current interactions, while the μ-like classification is relatively pure. For these reasons, only the μ-like sample is used in the analysis for multi-ring events.

The atmospheric event sample in the oscillation analysis is split further in sub-GeV ($E < 1.33\,\text{GeV}$) and multi-GeV ($E > 1.33\,\text{GeV}$) samples. At low energy the direction of the lepton and the neutrino are not well correlated. Therefore, the incoming neutrino direction is not well determined and the effects of oscillation are smeared out.

Even though SuperK is very big, high-energy muons or events close to the detector edge, will escape from the detector. Events which deposit all their energy inside the detector, mostly electrons (showering) and low energy muons, are classified as fully contained. If the interaction point is inside the inner detector but some particle (usually a muon) leaves the volume and has hits in the outer detector, the event is classified as partially contained. As only a part of the energy is detected, the energy resolution is worse for partially contained events. After applying all selection criteria to reduce the atmospheric-muon background, the remaining partially-contained sample is mostly due to ν_μ interactions.

To increase the event sample, one can also detect neutrino events inside the rock surrounding the detector. These events are indistinguishable from atmospheric muons, but as no muon can penetrate the earth, muons which enter the detector from below the horizon can only be due to neutrino interactions. This event sample is called the upward-muon sample. Muon tracks of at least 7 m long in the inner detector with an upward direction are selected. A manual scan of the events is needed to remove the remaining atmospheric-muon background.

The backgrounds to the various event samples are different. The common background from internal radioactivity is removed by the visible energy cut at $E > 30\,\mathrm{MeV}$. Atmospheric muons are removed by not allowing hits in the outer detector. The remaining background in the fully-contained sample is below 1 % and mostly from PMT flasher events and partially from neutrons and not-vetoed atmospheric muons. The neutrons generate an e-like signal via the interaction chain $p + n \rightarrow d + \gamma$, followed by Compton scattering $\gamma + e^- \rightarrow \gamma' + e^-$. In the partially-contained sample, the background is mainly due to not-vetoed atmospheric muons, but only at the 0.2 % level. For the upward-muons near the horizon, horizontal atmospheric muons can be reconstructed accidentally as upward muons or appear to go upward due to multiple-Coulomb scattering. As the rock overburden has two weaker shielding regions, the first analysis bin with $-0.1 < \cos\theta < 0$ is corrected for the remaining atmospheric-muon background.

Solar-neutrino detection

Solar neutrinos are detected via the strongly forward-peaked neutrino–electron scattering interaction which is mainly sensitive to ν_e (see section 1.2.4). While the high-energy ν_e interactions from atmospheric neutrinos are easily recognized from their Cherenkov ring, the solar-neutrino interactions are much more difficult to extract from the background, even though their flux is much higher. The low-energy solar neutrinos give a maximum electron recoil energy of about 18 MeV. These electrons do not form clear rings of hit PMTs, as the number of detected Cherenkov photons is only about 7 hits per MeV. Furthermore, the background at low energies is high, especially below 6.5 MeV where most natural radioactivity takes place. The event trigger requires a certain number of hit PMTs in a 200 ns time window and therefore effectively acts as an energy threshold. Due to the rapidly rising background at lower energies, the energy threshold is determined by the maximum allowed trigger rate. The trigger threshold has been gradually decreased between 1996 (6.5 MeV) and 2000 (4.5 MeV) with the installation of more and faster computers. These computers are used online to select events whose vertex is reconstructed inside the fiducial volume. Because of the energy threshold, SuperK is only sensitive to a very small fraction of the solar-neutrino flux, namely the high-energy ^{8}B neutrinos. The endpoint energy is about 14 MeV for these neutrinos. The standard-solar-model prediction (BP2004) for the ^{8}B neutrino flux is $5.79 \cdot 10^6\ \nu\ \mathrm{cm}^{-2}\,\mathrm{s}^{-1}$ [95], which corresponds to an expected detection rate in SuperK of 325.6 events per day.

The vertex position is reconstructed from the PMT timing information with a resolution of about 200 cm. The recoil electrons from neutrino–electron interactions create only a very short track of maximum a few centimeters. The direction of this track can not be determined from its begin and end-point. Instead, the direction of the electron is measured from the ring-pattern of the Cherenkov light with about 25° accuracy. The electron energy is correlated to the number of PMT hits corrected for water transparency and light propagation. The energy resolution runs from 18 % at 5 MeV to 12 % at 20 MeV.

A linear electron accelerator has been used to inject 5 to 16 MeV electrons at precise locations to calibrate vertex, direction and energy resolution. Stopping muons and ^{16}N β-decays are used to calibrate the absolute energy scale.

Except for the already mentioned background from radon, the main background below 6.5 MeV comes from radioactivity in the surrounding rock and from the detector material. This background is suppressed by requiring a minimum distance between the vertex and the detector wall. Above 6.5 MeV, the main background is from muon-induced spallation, already discussed at the beginning of this section. A remaining small background is due to beta-gamma decays of ^{16}N created by μ^- capture on ^{16}O.

1.6.2 SNO

The inner detector of the SNO experiment consists of a spherical, 12 m diameter, acrylic vessel filled with 1000 ton pure heavy water (D_2O). It is suspended in the outer detector which is a 22 m diameter and 34 m high cylinder filled with normal water (H_2O). The SNO detector is sensitive to three interaction processes of solar neutrinos: $\nu_x + e^- \rightarrow \nu_x + e^-$ (ES), $\nu_e + d \rightarrow 2p + e^-$ (CC), and $\nu_x + d \rightarrow p + n$ (NC). The charged-current ν_e interaction on deuterium has an energy threshold of 1.442 MeV. The neutral-current disintegration of the deuteron is independent of neutrino flavour and makes a measurement of the total flux possible. This measurement is only sensitive to the ^{8}B and `hep` neutrinos which have an energy spectrum extending above the 2.224 MeV dissociation threshold.

The electrons from the CC and ES interactions are detected by the Cherenkov light they generate in the water. The neutron from the NC reaction is captured by a nucleus with high-energy photons carrying away the released binding energy. In the first phase of the SNO experiment, the inner detector was filled with pure heavy water; in the second phase, 2000 kg of salt (NaCl) was added to the heavy water. The addition of salt enhances the NC detection efficiency, because of the much larger cross-section for neutron capture on ^{35}Cl compared to ^{2}H. Therefore, the neutron is captured closer to its production point and has less chance of leaving the detector. The photons from the neutron capture are detected indirectly by the Cherenkov light of an atomic electron released by Compton scattering. The signals of the three reactions are therefore not that different from each other as all are detected from the Cherenkov light emitted by electrons. The SNO experiment measures four parameters for each event: the total deposited energy (T_{eff}), the angle with the sun ($\theta_\odot$), the isotropy of the distribution of light in the 4π solid angle (β_{14}), and the radial position of the event inside the detector (ρ). The three different processes and backgrounds have (slightly) different distributions of these four variables. A global fit to the measured distributions of the four variables extracts the relative contributions from ES, NC, CC and background interactions as function of energy. Figure 1.14 shows these distributions for the three different signals and the main background from external neutrons [114].

The ρ distribution allows one to subtract the background from external neutrons entering the inner detector. The ES interaction maintains the directionality. The CC reaction produces an electron with an energy highly correlated with that of the neutrino and is therefore sensitive to deviations from the expected energy spectrum. The capture of neutrons from the NC reaction on ^{35}Cl releases 8.6 MeV energy in on average 2.5 photons, compared to the single 6.25 MeV photon from the capture on ^{2}H. Multiple photons give rise to a more isotropic distribution of light from multiple Compton electrons. This higher isotropy shifts the β_{14} distribution for the NC reaction to lower values with respect

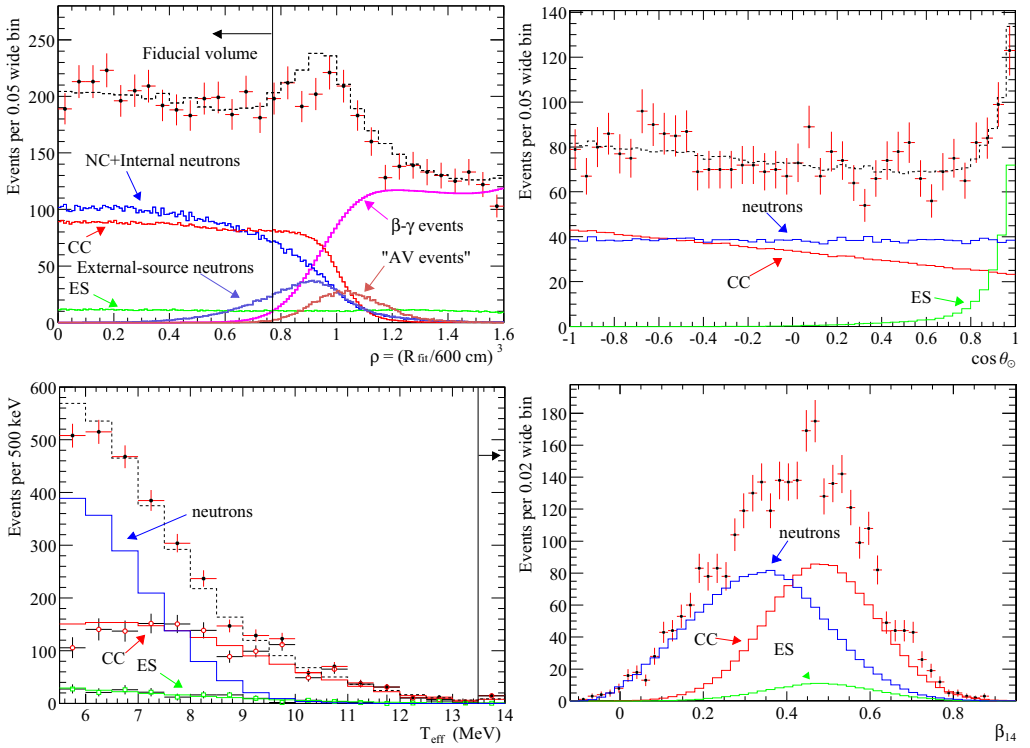

Figure 1.14: The contributions of the three different physics signals to the distributions of the four experimental variables in SNO. The solid lines are from Monte-Carlo calculations and the dashed line is the sum of all contributions. The crosses show the actual data. The fluxes derived from neutrino–electron scattering (ES), charged-current (CC) and neutral-current (NC) interactions of solar ^{8}B neutrinos are extracted from a global fit to the data for these four distributions. Some of the background is due to radioactive inclusions in the acrylic containment vessel, indicated by the abbreviation AV.

to the data with capture on ^{2}H and therefore enables a better separation between the NC and CC signals. An energy cut at 5.5 MeV removes most of the low-energy internal radioactivity from the thorium and uranium decay chains. The main background to the NC signal is photo-dissociation of deuterium. By keeping the radon contamination as low as possible, this background was kept small. The calculated background from photo-dissociation in the total sample of 4722 events is 102 events [115].

1.6.3 KamLAND

The KamLAND experiment utilizes a similar technique as was used to prove the existence of the neutrino by Cowan and Reines (section 1.1.1). This time, though, the nuclear reactors are much further away. The KamLAND experiment is situated in the cavern previously used for the Kamiokande experiment, more or less in the middle of Japan's main island, whereas most nuclear reactors in Japan are placed along the coastline. About 80 % of the flux at the KamLAND site is from 26 reactors at distances between

134 km and 214 km with a weighted average of 180 km. This relatively narrow band of baseline distances makes it possible for KamLAND to study neutrino oscillation as function of energy.

The detector is a 13 m diameter balloon filled with liquid scintillator. The balloon is suspended in non-scintillating oil inside a 18 m diameter steel vessel, which itself is placed inside a cylindrical water-Cherenkov detector, the outer detector. The charged-current $\overline{\nu}_e$ interaction with protons, $\overline{\nu}_e + p \rightarrow e^+ + n$, generates direct scintillation light from the positron and its rapid annihilation (prompt energy deposit), followed by the delayed signal from neutron capture on hydrogen, giving a 2.2 MeV gamma. Using scintillator and high photo-cathode coverage of the inner detector makes a good measurement of the positron energy and the neutron capture gamma energy possible. The energy resolution is about $\Delta E/E \approx 7\,\%/\sqrt{E/\mathrm{MeV}}$. As the recoil energy of the neutron is small, the measured positron energy is correlated with the neutrino energy.

The energy spectrum for the neutrinos from the neutron-rich fission products in the nuclear reactors goes up to about 10 MeV and peaks around $E_{\overline{\nu}_e} = 4\,\mathrm{MeV}$. Anti-neutrinos from ^{238}U and ^{232}Th decays in the earth's core have $E_{\overline{\nu}_e} < 2.49\,\mathrm{MeV}$ and are suppresed by selecting events which have $2.6\,\mathrm{MeV} < E < 8.5\,\mathrm{MeV}$ together with a time and spatial coincidence for the neutron capture.[4] The delayed signal must occur within a time-interval of 0.5 μs to 1000 μs, take place within a distance of 2 m of the primary interaction point, and have an energy compatible with neutron capture on ^{1}H ($1.8\,\mathrm{MeV} < E < 2.6\,\mathrm{MeV}$).

The delayed coincidence technique with the applied energy window removes almost all background. The largest background is from muon-induced nuclear spallation and subsequent decays by positron and neutron emission ($\approx$ 3000 events per day). A veto of 2 ms after a passing muon eliminates most of this background, except for the slow neutron emitters, ^{9}Li and ^{8}He, which are suppressed by applying a 2 second time and 3 m spatial window around a passing muon.

1.7 Status of oscillation research

1.7.1 Atmospheric neutrinos

The discrepancies in measured ratios for atmospheric neutrinos between the water-Cherenkov and iron-calorimeter experiments, have been investigated by the Soudan experiment, running between 1990 and 1999. The Soudan detector consisted of an iron calorimeter surrounded by a veto shield. It found $R_{\mathrm{atm}} = 0.64 \pm 0.11(\mathrm{stat}) \pm 0.06(\mathrm{sys})$ [96], similar to the KamII and IMB results. It also showed that neutron-induced background could not explain the difference between the water-Cherenkov and iron-calorimeter detectors [97]. A different analysis for upward-going muons with $E > 1\,\mathrm{GeV}$ gave much less stringent limits for $\nu_\mu \rightarrow \nu_\tau$ oscillation [98] and is in contradiction with the previous IMB result for upward muons [85].

The latest results on atmospheric neutrinos come from the SuperK and MACRO experiments. SuperK is described in section 1.6.1. MACRO is a large underground iron calorimeter. The results of MACRO are in agreement with the SuperK results [99]. The MINOS experiment has published preliminary results for its atmospheric-neutrino measurement.

[4] The low background in the detector and a special selection of low-energy events has enabled KamLAND to detect these so-called geo-neutrinos [92].

The magnetic field of the MINOS detector makes it possible to separate atmospheric ν_μ and $\overline{\nu}_\mu$ [100]. As the earlier mentioned discrepancies (see section 1.4.3) have now been clarified and the SuperK experiment yielded the most accurate results, this section only discusses the latest SuperK results of Ref. 101.

Zenith angle dependence

In accordance with earlier atmospheric-neutrino measurements, the simplest analysis gives the result as the data over Monte-Carlo ratio for the ratio $(\nu_\mu + \overline{\nu}_\mu)/(\nu_\mathrm{e} + \overline{\nu}_\mathrm{e})$. This ratio yields for the latest data 0.67 ± 0.1 using a weighted average over all event categories. In the next step, one looks at the dependence of the muon and electron-neutrino flux on the baseline. The baseline is determined by the incoming neutrino direction and the earth's diameter. The main result is the up/down ratio (up $\equiv \cos\theta < -0.2$, down $\equiv \cos\theta > +0.2$) which turns out to be approximately 1 for low-energy μ-like events and for low and high-energy e-like events. The up/down ratio for high-energy μ-like events is, however, only about a half. At high energy the flux is believed to be isotropic and so this ratio should be 1 if every neutrino entering the earth is also leaving it, independent of any production model. A value below 1, clearly indicates that neutrinos are disappearing on their way through the earth.

In 1489 days of acquiring data, the SuperK experiment has collected enough events, 4099 e-like, 5436 μ-like and 2259 upward muons, to perform a more detailed analysis based on energy and baseline. At high neutrino energies, there is good correlation between the neutrino and lepton direction. Below $400\,\mathrm{MeV}/c$ the correlation between the neutrino and lepton direction is such that any effects depending on the baseline will be washed out. The results of the analysis as function of zenith angle for the different event categories are shown in Figure 1.15. The data show a clear deficit with respect to the Monte-Carlo expectation for μ-like events at higher energies and longer baselines. The number of e-like events are compatible with the Monte-Carlo, which suggest that the disappearance of ν_μ is not creating any ν_e. The data can be fitted very well assuming $\nu_\mu \rightarrow \nu_\tau$ oscillation, indicated by the solid lines, as discussed later.

The number of events is large enough to make a sub-selection of events which each have a small uncertainty in the L/E ratio. This sub-set is used to study the L/E dependence of the ν_μ flux, which should show the characteristic oscillation pattern. To see the maximal oscillation dip requires a good measurement of both L and E. The sub-set is taken from the ν_μ charged-current events in the fully and partially-contained event samples. The selection requires that $\Delta(L/E) < 70\,\%$ and is based on the Monte-Carlo calculation of $\Delta(L/E)$ for a given zenith angle and energy. In general, events with $|\cos\theta| < 0.1$ have large ΔL and events with $E < 1\,\mathrm{GeV}$ have large $\Delta\theta$ and therefore also large ΔL. In the partially-contained sample, muons that stop in the outer detector have good ΔE, while escaping muons have bad ΔE. In general, any event with $E > 50\,\mathrm{GeV}$ will leave the detector and is not selected.

For the selected 40 % of fully-contained and 70 % of partially-contained events, one can plot the ratio of the number of measured versus expected events as function of L/E, as is depicted in Figure 1.16 [102]. The characteristic dip, corresponding to the first oscillation maximum, occurs around $L/E = 500\,\mathrm{km/GeV}$. The data can be fitted well with two-flavour $\nu_\mu \rightarrow \nu_\tau$ oscillation, but disfavour at $3.4\,\sigma$ and $3.8\,\sigma$ the alternative explanations of neutrino decay [103] and decoherence [104].

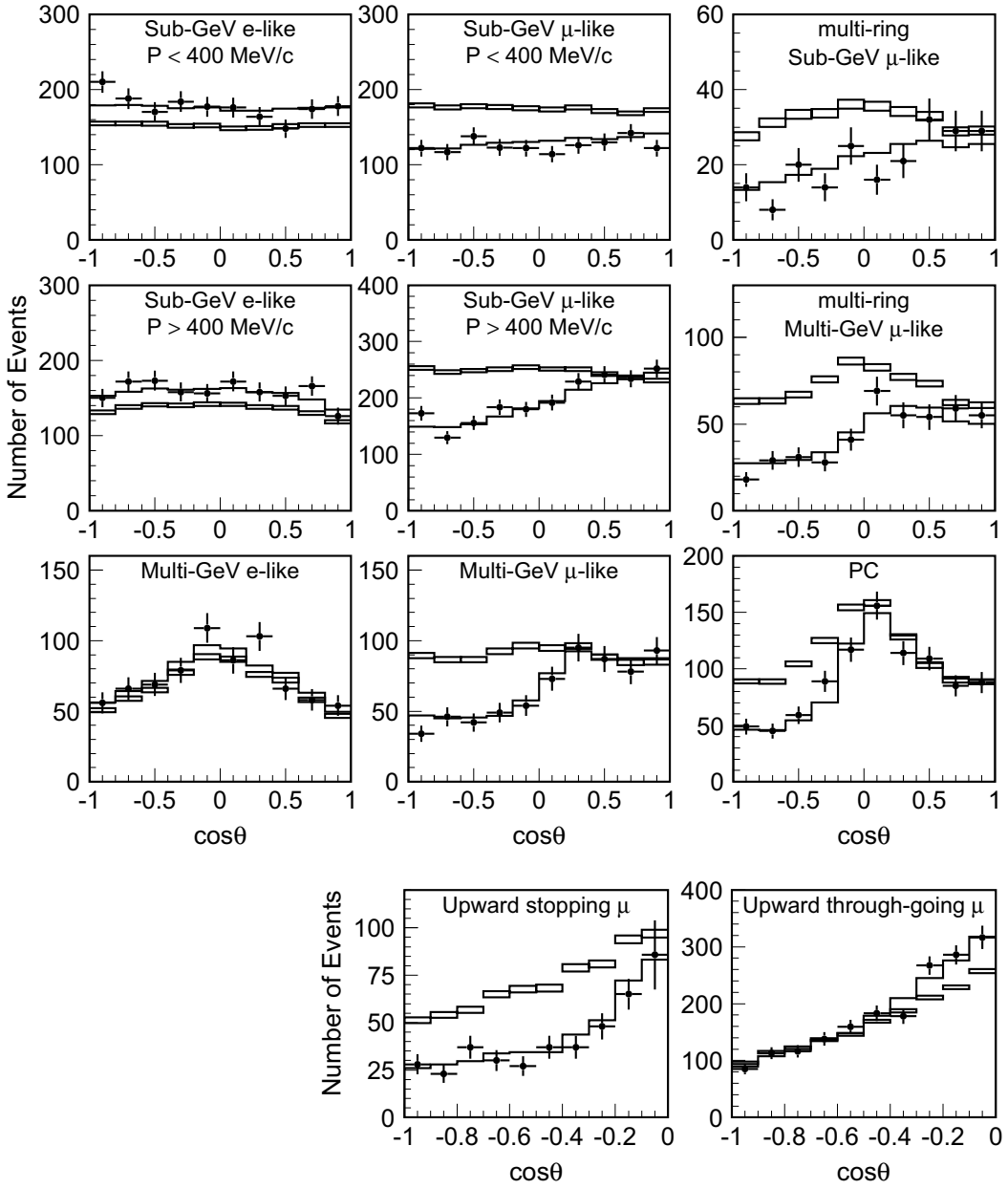

Figure 1.15: The zenith angle distribution for the different event categories of Super-Kamiokande. The e-like events are in accordance with the Monte-Carlo, while the μ-like events clearly deviate from the Monte-Carlo depending on the flight length given by $\cos\theta$. The crosses show the data, the boxes show the Monte-Carlo expectation without oscillation and the solid lines the best-fit expectations for $\nu_\mu \to \nu_\tau$ oscillation with $\sin^2(2\theta) = 1$ and $\Delta m^2 = 2.1 \cdot 10^{-3}\,\mathrm{eV}^2$. The definition of the different event classes can be found in Ref. 101.

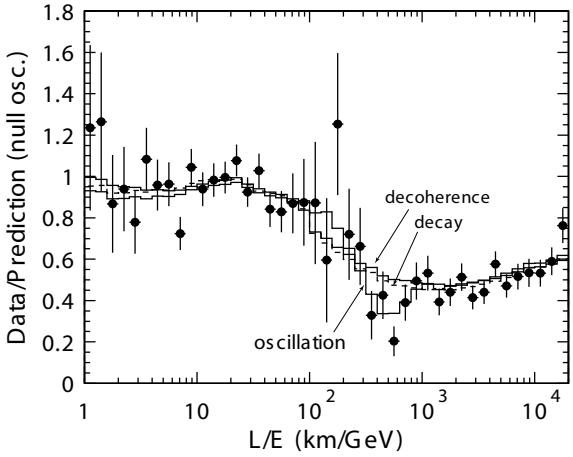

Figure 1.16: The data over Monte–Carlo ratio of atmospheric ν_μ (μ-like events) interaction rate as function of L/E for a sub-sample of events with small uncertainty of L/E. The crosses show the measured rate and the solid line the best fit for $\nu_\mu \to \nu_\tau$ oscillation. Also shown are fits for neutrino decoherence and decay.

Oscillation parameters

From the above results, one can conclude that the oscillation is not ν_μ to ν_e, as there is no surplus of upward electron neutrinos. The natural assumption is then that ν_μ oscillates to ν_τ. Interactions of ν_τ are largely invisible in SuperK due to a charged-current threshold of about 3.5 GeV, although some ν_τ interactions could end up in the multi-GeV e-like sample, which has been excluded from the oscillation analysis.

Extraction of the oscillation parameters involves a fit of the data versus Monte-Carlo, with Δm^2 and $\sin^2(2\theta)$ as parameters in the Monte-Carlo. The simulated events are classified in bins for ν_e or ν_μ interactions, energy, and flight length. Fits to all data and for the separate categories give favoured parameter regions which are shown in Figure 1.17 [101]. For the combined fit, the 90 % confidence-level intervals for $\nu_\mu \to \nu_\tau$ oscillation parameters are $\sin^2(2\theta) > 0.92$ and $1.5 \cdot 10^{-3} < \Delta m^2 < 3.4 \cdot 10^{-3}\,\mathrm{eV}^2$. The separate analysis in terms of L/E gives similar results with slightly smaller uncertainty for Δm^2: $\sin^2(2\theta) > 0.90$ and $1.9 \cdot 10^{-3} < \Delta m^2 < 3.0 \cdot 10^{-3}\,\mathrm{eV}^2$.

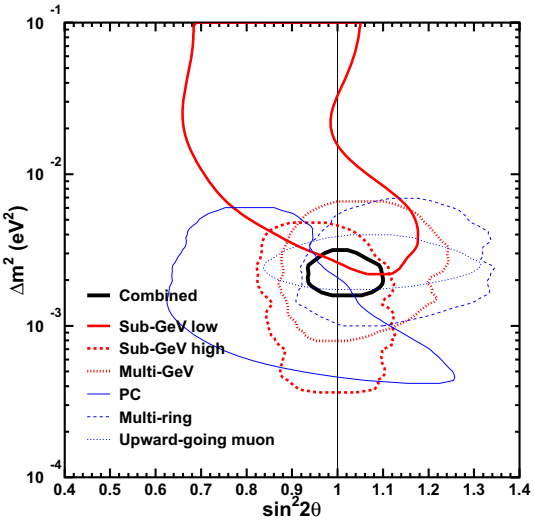

Figure 1.17: Allowed 90 % confidence regions for $\nu_\mu \to \nu_\tau$ oscillation parameters extracted from different event categories of SuperK and for the combined analysis.

Alternatively, ν_μ could oscillate to a hypothetical sterile neutrino (ν_s). Sterile neutrinos have no charged-current or neutral-current interactions and therefore show up as pure ν_μ disappearance. However, an earlier analysis by SuperK has shown that oscillation to ν_s can be excluded at the 99 % confidence level for the current oscillation parameters [105]. The difference due to the absence of neutral-current interactions for ν_s is exploited in two ways. First, in the low-energy, multi-ring, fully-contained sample, the e-like events contain about 30 % hadron (pion) showers from neutral-current events. Part of these events would be absent if ν_μ would oscillate to ν_s instead of to ν_τ. Second, the earth's matter would cause a MSW effect (see section 1.3.2) for $\nu_\mu \to \nu_s$. This effect is invisible for $\nu_\mu \to \nu_\tau$ because they have identical neutral-current interactions. For $\nu_\mu \to \nu_s$, the oscillation parameters are changed by a factor 2 in the earth at $E_\nu = 15\,\text{GeV}$ and $\Delta m^2 = 3 \cdot 10^{-3}$. However, no effects are seen in the zenith angle distribution for the partially-contained sample with $E > 5\,\text{GeV}$, nor for the high-energy upward-muon sample.

1.7.2 Solar and reactor neutrinos

The results from the radio-chemical solar-neutrino experiments, Homestake, SAGE, Gallex and GNO, have not changed very much since 1992 [106–109]. In the mean time, though, both Gallex and SAGE have performed calibrations with an intense ^{51}Cr (Gallex and SAGE), ^{71}As (Gallex) and ^{37}Ar (SAGE) neutrino sources. These calibrations showed that the reported detection efficiencies and thus the solar-neutrino rates are understood [110–113]. All the Gallium experiments report a solar-neutrino rate of about 70 ± 6 SNU, which is only 54 % of the SSM prediction. The final Homestake result is 2.56 ± 0.23 SNU, which is only 0.3 of the SSM prediction. The latest result for the solar ν_e flux from SNO and SuperK are published in Refs. 114–116. These results are related via the CPT theorem with the KamLAND reactor $\overline{\nu}_e$ result [117,118], which will be described before the combined results for ν_e oscillation is given at the end of this section.

Before the measurements from SuperK, SNO and KamLAND, several solutions to the solar-neutrino disappearance, as measured by the radio-chemical and Kamiokande experiments (see section 1.4.2), were possible. These solutions defined four different regions in the $\sin^2(2\theta)$, Δm^2 plane for $\nu_e \to \nu_\mu/\nu_\tau$ oscillation:

Solution's name	Abbreviation	$\sin^2(2\theta)$	$\Delta m^2[\text{eV}^2]$
Large mixing angle	LMA (MSW)	$\approx 3/4$	$\approx 2 \cdot 10^{-5}$
Small mixing angle	SMA (MSW)	$\approx 6 \cdot 10^{-3}$	$\approx 5 \cdot 10^{-6}$
Low mass difference	LOW (MSW)	≈ 1	$\approx 8 \cdot 10^{-8}$
Vacuum oscillation	VAC	$\approx 3/4$	$\approx 10^{-10}$

In general MSW is important for $10^{-9} \lesssim \Delta m^2/E \lesssim 10^{-5}\,\text{eV}^2/\text{MeV}$. For Δm^2 in the MSW range, the oscillation length is much smaller than the distance sun–earth and propagation of neutrino mass-eigenstates is therefore incoherent. The detection probability at earth is then given by:

$$P(\nu_e) = P(\nu_1)\,\langle\nu_1|\,\nu_e\rangle + P(\nu_2)\,\langle\nu_2|\,\nu_e\rangle$$

where $P(\nu_1)$ and $P(\nu_2)$ are the probabilities for a solar ν_e to leave the sun as ν_1 respectively ν_2. For $\Delta m^2/E$ smaller than $10^{-9}\,\text{eV}^2/\text{MeV}$ the distance sun–earth approaches the oscillation length and the propagation should be treated coherent. In the case of the

VAC solution, one reverts to the earlier survival-probability formula of equation (1.8):

$$P(\nu_e) = 1 - \sin^2(2\theta)\,\sin^2\left(\pi\frac{L}{L_{osc}}\right)$$

SuperK

Between May 1996 and July 2001, SuperK recorded about 35 million solar-neutrino triggers. The event selection reduces this with about a factor 120 to about 300,000 solar-neutrino candidate events. This sample still contains about a factor 10 more background than signal. The signal is extracted from the background using the directionality of the neutrino–electron scattering process. The cross-section peaks at forward angles and the solar-neutrino interactions are therefore correlated with the direction of the sun. The background on the other hand is largely isotropic. The signal contribution can therefore be extracted as the surface of the forward peak in the distribution of the measured event directions with respect to the sun. This distribution is shown in Figure 1.18 [116]. The peak contains $22404 \pm 226(\text{stat})^{+784}_{-717}(\text{syst})$ solar-neutrino events, which corresponds to a ^{8}B neutrino flux of $\phi_B = 2.35 \cdot 10^6 \pm 0.02(\text{stat}) \pm 0.08(\text{syst})\,\text{cm}^{-2}\text{s}^{-1}$ The measured flux is only 41 % of the SSM predicted flux.

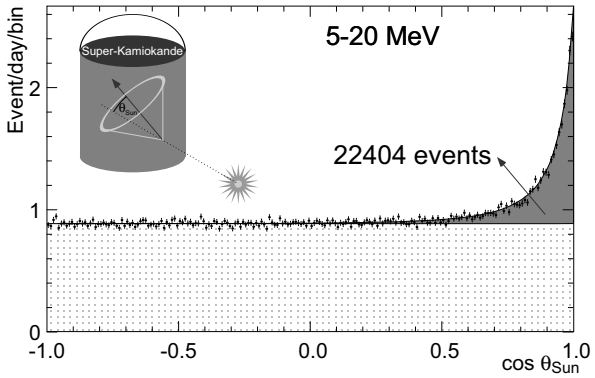

Figure 1.18: Number of solar-neutrino events as function of the angle with the sun's direction. The real solar-neutrino events show up as the forward peak on top of the uniform background.

Neutrino oscillation influences the SuperK measurements in three ways. First, the neutrino–electron scattering cross-section for ν_μ and ν_τ is only about $(1/6)^{\text{th}}$ of the cross-section for ν_e. Second, the neutrino energy spectrum is distorted because the ν_e survival probability, equation (1.8), is energy dependent. Changes in the spectrum translate directly to changes in the electron recoil-energy spectrum. Third, for the MSW solutions, the earth's matter influences the oscillation probability which would show up as a 24 hour modulation of the signal rate. For the VAC solution, on the other hand, the survival probability is baseline dependent which would show up as a seasonal fluctuation due to the eccentricity of the earth's orbit. With the large statistics of SuperK, it is possible to look for both energy dependence and time variations.

The SuperK data show no observable distortions from the expected shape of the ^{8}B neutrino spectrum. The seasonal variation is consistent with the expected $1/r^2$ behaviour at 69 % confidence level. This excludes the VAC solution for solar-neutrino oscillation. The day versus night asymmetry was measured to be $[2.1 \pm 2.0(\text{stat})\,^{+1.3}_{-1.2}(\text{syst})]$ %. This value is both consistent with zero and with the expected value for part of the LMA solution. It does exclude some of the LMA region at low Δm^2. A combined analysis

of the data as function of energy and zenith angle gives two allowed regions for the oscillation parameters at 95 % confidence level in the LOW and LMA regions, but excludes the SMA solution. The two allowed regions are depicted in Figure 1.19 [116]. From the χ^2 values, one can see that the best fit-point is in the LMA region at $\tan^2(\theta) = 0.52$ ($\Leftrightarrow \sin^2(2\theta) = 0.90$) and $\Delta m^2 = 7 \times 10^{-5}\,\mathrm{eV}^2$.

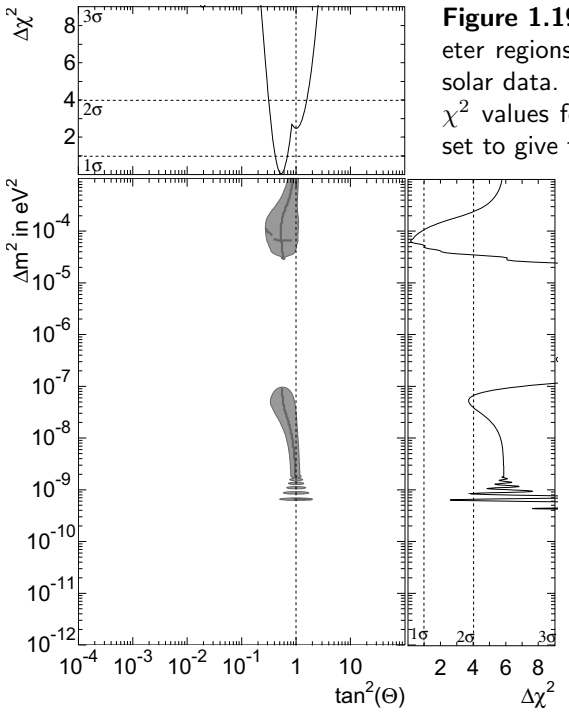

Figure 1.19: Allowed $\nu_e \to \nu_{\mu\tau}$ oscillation parameter regions at 95 % confidence level from SuperK solar data. To the top and right are indicated the χ^2 values for the fit when the other parameter is set to give the lowest χ^2 (lines inside the regions).

SNO

The detection principle of the SNO solar-neutrino measurement has been explained in section 1.6.2. The results, covering the period up-to September 2003, can be found in Refs. 114, 115. The SNO experiment has measured the charged-current, neutral-current and neutrino–electron scattering rate which have different contributions from ν_e and ν_μ or ν_τ interactions. For each interaction type, the measured flux and its uncertainty define bands of possible values in the $\nu_{\mu\tau}$ versus ν_e plane. The slopes of the bands are determined by the relative sensitivity of each process to ν_e and $\nu_{\mu\tau}$: charged-current $\propto \nu_e$; neutral-current $\propto \nu_e + \nu_{\mu\tau}$; and neutrino–electron scattering $\propto \nu_e + 0.16\nu_{\mu\tau}$. A combined fit to the four distributions of Figure 1.14 yields the relative amounts of charged-current, neutral-current, and neutrino–electron scattering rates. The ν_e and $\nu_{\mu\tau}$ fluxes derived from these numbers are shown in Figure 1.20 [115]. The measured charged-current rate gives a ^{8}B flux of:

$$\phi_B = \left(1.68 \pm 0.06(\mathrm{stat})^{+0.08}_{-0.09}(\mathrm{syst})\right) \times 10^6\,\mathrm{cm}^{-2}\mathrm{s}^{-1} \quad ,$$

which corresponds to only about $1/3^{\mathrm{th}}$ of the expected SSM flux [119, 120]. This result confirms the earlier radio-chemical experiments. However, the neutral-current measurement yields:

$$\phi_B = \left(4.94 \pm 0.21(\mathrm{stat})^{+0.38}_{-0.34}(\mathrm{syst})\right) \times 10^6\,\mathrm{cm}^{-2}\mathrm{s}^{-1} \quad .$$

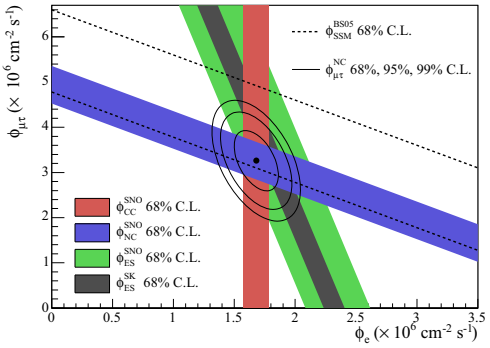

Figure 1.20: Solar ^{8}B neutrino flux, split in ν_e and $\nu_{\mu\tau}$ contributions, as measured by SNO from the charged-current (CC), neutral-current (NC) and neutrino–electron scattering (ES) rates. The width of the bands represent 1σ errors, the slopes correspond to the sensitivity for each process to ν_e and $\nu_{\mu\tau}$. The total ^{8}B neutrino flux (neutral-current result at $\phi_e = 0$) is within the 1σ expectation of the SSM (dashed lines).

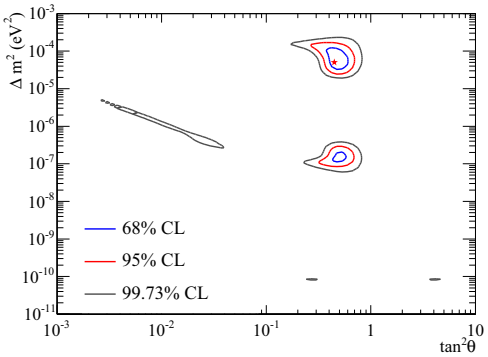

Figure 1.21: Allowed parameter regions at different confidence levels for solar-neutrino oscillation. The best fit point is indicated by the star and is in the LMA region. The LOW solution also gives 1σ fit probabilities. The SMA and VAC solutions are almost excluded except for some small regions at 3σ.

This value for the total neutrino flux lies within the range predicted by the SSM which has about 20 % uncertainty.

The SNO neutral-current result provides evidence for the hypothesis that the ν_e from ^{8}B decay are transformed into active neutrino species (ν_μ, ν_τ). The neutrino–electron scattering measurement further limits the range of the ν_e versus $\nu_{\mu\tau}$ flux ratio, especially if the measurement from SuperK is used, as is shown in Figure 1.20.

A fit which compares the data to the calculated propagation (and matter effects) of solar neutrinos for a given set of $\nu_e \rightarrow \nu_{\mu\tau}$ oscillation parameters gives regions of allowed parameters. These allowed regions at different confidence levels are shown in Figure 1.21. The best fit point is in the LMA region at $\Delta m^2 = 5.0 \cdot 10^{-5}\,\mathrm{eV}^2$ and $\tan^2(\theta) = 0.45$ ($\sin^2(2\theta) = 0.86$)). Also the LOW solution has a region which good χ^2 values. The SMA and VAC solutions are almost excluded as only some small 3σ regions remain.

KamLAND

Although KamLAND measures reactor $\overline{\nu}_e$, see section 1.6.3, its results are related to the solar-neutrino measurements via CPT invariance. The energy range of the reactor anti-neutrinos also matches the typical range of solar neutrinos. The last published result from the KamLAND experiment covers the data taken between March 2002 and January 2004. Based on the reactors power output, the expected number of events in the KamLAND experiment is 365.2 ± 23.7. Instead, only 258 events were detected, which corresponds to $[65.8 \pm 4.4(\mathrm{stat}) \pm 4.7(\mathrm{syst})]$ % of the expected number [117]. This number falls squarely in

the range predicted by the LMA solar-neutrino solution ($L_{\mathrm{osc}} \approx 130\,\mathrm{km}$), but is more than 4σ different from 1 which would be the case for the SMA, LOW and VAC solutions. The measured ratio and those from previous short-baseline reactor experiments are shown in Figure 1.22.

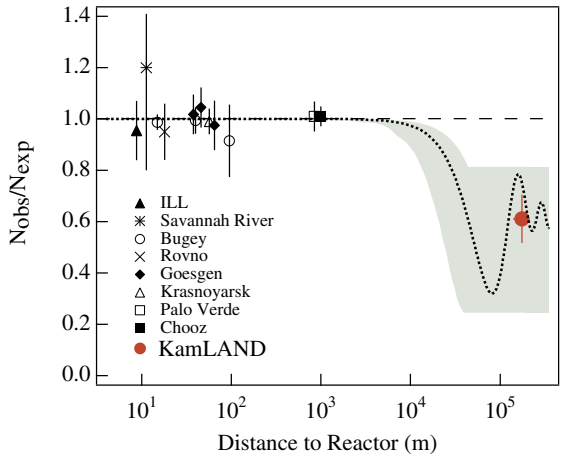

Figure 1.22: The ratio of measured over expected $\overline{\nu}_{\mathrm{e}}$ neutrino fluxes for several reactor experiments [118]. The result of KamLAND at $L = 1.8 \cdot 10^5\,\mathrm{m}$ shows the disappearance of $\overline{\nu}_{\mathrm{e}}$ at long baselines. The result is consistent with the expectation for the solar LMA solution (shaded area). The best fit for $\overline{\nu}_{\mathrm{e}} \rightarrow \overline{\nu}_{\mathrm{x}}$ oscillation yields $\Delta m^2 = 5.5 \cdot 10^{-5}\,\mathrm{eV}^2$ and $\sin^2(2\theta) = 0.83$ and is indicated by the dotted line.

If neutrino oscillation is responsible for the $\overline{\nu}_{\mathrm{e}}$ disappearance, KamLAND should be able to see a spectral distortion of the measured $\overline{\nu}_{\mathrm{e}}$ flux for a given range of Δm^2. Because about 80 % of the flux has a baseline of around 180 km, oscillation would give a relatively clear sinusoidal shape as function of energy (E). Figure 1.23 shows the survival probability as a function of L/E, with L fixed to 180 km. In the figure the first maximum and first two minima of the oscillation pattern can been seen. From the maximum at $L/E = 32\,\mathrm{km/MeV}$ one can directly derive Δm^2 which yields $\Delta m^2 = 7.7 \cdot 10^{-5}\,\mathrm{eV}^2$. The mixing angle determines the depth of the minima. From the figure one can estimate that $\sin^2(2\theta) \approx 0.7$. The limited statistics lead to large errors on the mixing angle. A precise fit of the KamLAND data yields $\Delta m^2 = 7.9^{+0.6}_{-0.5} \times 10^{-5}\,\mathrm{eV}^2$ and $\sin^2(2\theta) = 0.86^{+0.14}_{-0.30}$.

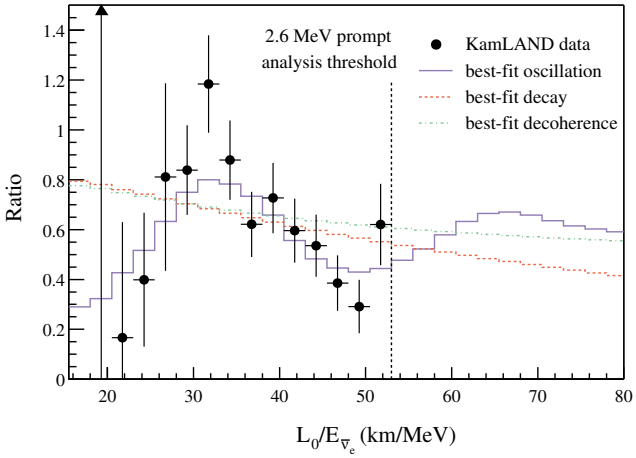

Figure 1.23: Dependence of the ratio of the measured neutrino-rate versus the expected rate in the KamLAND experiment as function of energy. In this analysis, all reactor neutrinos are assumed to come from a single reactor at $L_0 = 180\,\mathrm{km}$ [117].

Combined solar results

One can take all solar-neutrino measurements together to limit the possible oscillation parameters further. In such an analysis, KamLAND's Δm^2 measurement limits the solution to the LMA region. KamLAND also has the best determination of Δm^2 from the spectral distortion in the L/E measurement. The mixing angle is best determined by SuperK and SNO. In Table 1.2 a summary of the results is given as well as the average of the combined results as reported in Refs. 115–117. The allowed parameter region for the combined result at different confidence levels is shown in Figure 1.24 [145].

	$\Delta m^2 \left[10^{-5}\,\mathrm{eV}^2\right]$	$\sin^2(2\theta)$	$\tan^2(\theta)$	$\phi_\mathrm{B}\ \left[10^6\,\mathrm{cm}^{-2}\mathrm{s}^{-1}\right]$
SNO	$5.0\,^{+6.2}_{-1.8}$	$0.86\,^{+0.06}_{-0.09}$	$0.45\,^{+0.11}_{-0.10}$	5.11
SuperK	$6.3\,^{+4.7}_{-2.1}$	$0.90\,^{+0.07}_{-0.08}$	$0.52\,^{+0.18}_{-0.12}$	-
	$7.6\,^{+4.4}_{-2.3}$	$0.90\,^{+0.07}_{-0.08}$	$0.52\,^{+0.18}_{-0.12}$	-
solar (combined)	$6.5\,^{+4.4}_{-2.3}$	$0.86\,^{+0.05}_{-0.07}$	$0.45\,^{+0.09}_{-0.08}$	5.06
KamLAND	$7.9\,^{+0.6}_{-0.5}$	$0.86\,^{+0.14}_{-0.30}$	$0.46\,^{+0.54}_{-0.26}$	-
solar + KamLAND	$8.0\,^{+0.6}_{-0.4}$	$0.86\,^{+0.05}_{-0.06}$	$0.45\,^{+0.09}_{-0.07}$	4.92

Table 1.2: Oscillation parameters from separate and combined results of solar ν_e experiments and the KamLAND experiment.

1.7.3 Accelerator experiments

The results from earlier accelerator neutrino experiments will not be mentioned here, as they are all superseded by the positive results from solar and atmospheric experiments. The discussion is limited to the confirmation of ν_μ disappearance by the K2K experiment and the unconfirmed positive oscillation result from LSND.

The K2K experiment is a combined near and far detector experiment in Japan [121]. It uses an accelerator ν_μ beam, generated at the KEK laboratory, pointing to the SuperK detector which is located at a distance of 250 km. The near detector is a smaller copy of the SuperK detector with additional fine-grained detectors. The near detector is used to accurately measure the neutrino flux. The short-spill timing of the beam allows to detect any beam related ν_μ interactions in SuperK with negligible background. The experiment reported a statistical significant deficit of ν_μ interactions: 107 events detected while 151 ± 11 were expected from the measured flux at the near detector [122]. This result is consistent with the oscillation parameters determined from atmospheric $\nu_\mu \to \nu_\tau$ oscillation.

One other experiment, with a near and a far detector, will also give results in the near future. The MINOS experiment in Soudan (USA), has just published its preliminary results. An observed disappearance of ν_μ [123] over the 735 km baseline from Fermilab's main injector confirmed the result of K2K. The oscillation parameters derived from these data are compatible with the SuperK atmospheric-neutrino measurements. The MINOS experiment has reached similar uncertainties as the SuperK experiment. With more data to come, the MINOS experiment will be able to determine the oscillation parameters with an uncertainty of less than 10 %. Another long-baseline experiment, OPERA [124], will

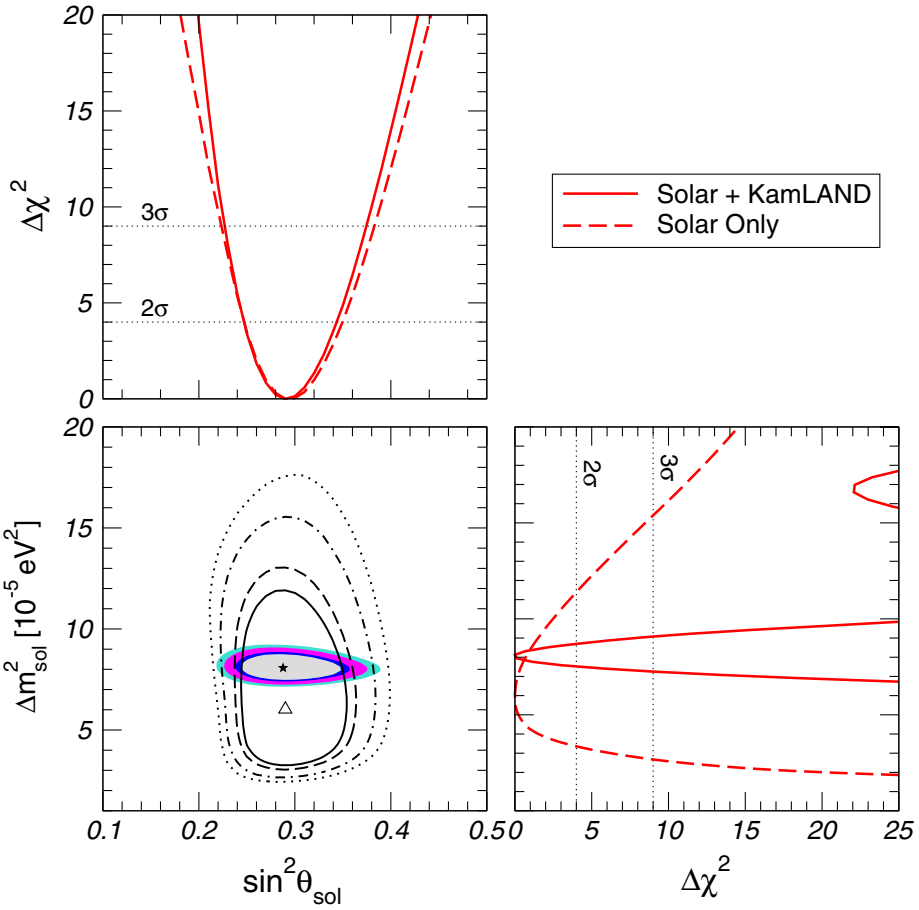

Figure 1.24: Allowed oscillation parameter regions from all solar and KamLAND results combined. The overlap between these results limits the solution to the LMA region. The selected part of the KamLAND result (filled areas) constrains Δm^2, while the solar experiments (filled and dashed lines) limit the mixing angle. The independent best-fit points are indicated by the star and triangle symbols. The plots on top and to the right show the χ^2 of the overall fit when the other parameter is optimized separately and indicate the uncertainty in the result.

become operational in 2007 at Gran-Sasso in Italy. This experiment plans to detect ν_τ events using emulsion in a high-energy ν_μ beam coming from CERN, 732 km away.

In the future, the planned T2K [125] experiment in Japan, will have a baseline of 295 km from an accelerator to be built at Tokai (near Tokyo) to the SuperK detector. The T2K experiment will make precision measurements of ν_μ disappearance and possibly ν_e appearance using a high-intensity neutrino beam. The neutrino energy is tuned to have the first oscillation maximum occuring at the SuperK distance of 295 km.

The reason some experiments have been looking for possible sterile neutrinos is the claim for a positive oscillation signal from the LSND experiment [126–128]. Between 1993 and 1998, LSND used the delayed neutron-signal coincidence technique to look for

$\overline{\nu}_e$ interactions ($\overline{\nu}_e + p \rightarrow e^- + n$) at a continuous, low-energy, neutrino source. The neutrinos are generated from decay-at-rest of π^+ and μ^+ stopped inside a beam dump. Negative pions and the few μ^- from decay in flight of π^- are mostly captured before decaying. Therefore, only ν_μ from π^+ decays and $\overline{\nu}_\mu$ and ν_e from μ^+ decays escape the beam dump. Hence, there are almost no $\overline{\nu}_e$ present in the beam ($\phi(\overline{\nu}_e)/\phi(\overline{\nu}_\mu) = 8 \cdot 10^{-4}$). The LSND detector was located 30 m behind this beam dump. The experiment reported an excess of 87.9 ± 23.2 $\overline{\nu}_e$ events with respect to the expected background of 30 ± 6 events. If interpreted as due to oscillation from $\overline{\nu}_\mu$, the oscillation probability would be $[0.264 \pm 0.067(\text{stat}) \pm 0.045(\text{sys})]\,\%$ [128]

However, most of the preferred oscillation region is excluded by other experiments, such as short-baseline reactor experiments and the KARMEN experiment. The KARMEN detector used a similar neutrino source as LSND, but with a pulsed beam. Their detector was placed perpendicular to the beam-dump and had a shorter baseline of 17 m. The KARMEN experiment did not see an excess of $\overline{\nu}_e$ events [129]. A combined analysis of the KARMEN and LSND data shows that only a small region with Δm^2 between 0.1 and 0.7 eV^2 and $\sin^2(2\theta) \approx 10^{-3}$ remains [130]. This region is incompatible with both the solar and atmospheric oscillation results. A fourth neutrino state would be needed to explain all oscillation results. This fourth neutrino state must be sterile because the number of light neutrinos coupling to the Z^0 is only three (see section 1.1.3). The MiniBooNE experiment should confirm or reject the LSND signal in the near future [131].

1.7.4 Cosmic neutrinos

The field of neutrino astronomy commenced with the detection by the Kamiokande-II and IMB experiments of neutrinos from the 1987 supernova in the Large Magellanic Cloud (distance $\approx 1.7 \cdot 10^{18}$ km) [132–135]. The cluster of detected events is shown in Figure 1.25 [134]. Nowadays, several collaborations are constructing enormous detectors to detect the very low fluxes of cosmic neutrinos using Cherenkov radiation. These detectors use large volumes of water deep in the sea (BAIKAL [136], ANTARES [137], NESTOR [138], and NEMO [139]) or a large volume of ice several kilometers down at the south pole (AMANDA [140] and its successor ICECUBE [141]). Other experiments and proposals exist to detect coherent radio-waves emitted by large electro-magnetic showers in either the south-pole ice, RICE [142] and ANITA [143], or from the moon, GLUE [144].

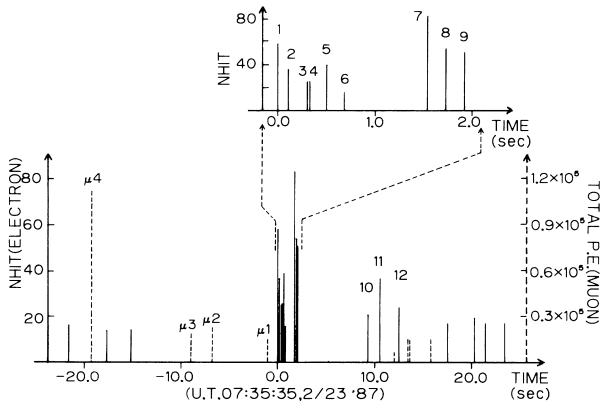

Figure 1.25: All events seen in the Kamiokande-II detector within a 45 second window around the time of supernova SN1987A. The height of each line represents the measured energy. Solid lines are electron-like events (left scale) and dashed lines atmospheric muons crossing the detector (right scale). A burst of electron neutrinos is seen at $t = 0$ s.

1.7.5 Three-flavour oscillation

The results of atmospheric and solar neutrino experiments can be fitted well in a theory with two-flavour neutrino oscillations dominated by small mass differences and high mixing angles. As there are three neutrino flavours, the results of all experiments should be analysed in a three-flavour oscillation theory. The results of all the experiments, except for LSND, can be fitted in such a model with the oscillations dominated by almost the same two small mass differences and mixing angles [145, 146]. However, for the three-flavour mixing matrix, one of the mixing angles remains unknown. Assuming a unitary mixing matrix for three neutrino flavours, the complete mixing matrix can be written as the product of three matrices:

$$U = \begin{pmatrix} 1 & 0 & 0 \\ 0 & c_{23} & s_{23} \\ 0 & -s_{23} & c_{23} \end{pmatrix} \times \begin{pmatrix} c_{13} & 0 & s_{23}\, e^{i\delta} \\ 0 & 1 & 0 \\ -s_{13}\, e^{i\delta} & 0 & c_{23} \end{pmatrix} \times \begin{pmatrix} c_{12} & s_{12} & 0 \\ -s_{12} & c_{12} & 0 \\ 0 & 0 & 1 \end{pmatrix} \quad ,$$

with $c_{\alpha\beta} = \cos\theta_{\alpha\beta}$ and $s_{\alpha\beta} = \sin\theta_{\alpha\beta}$. The first matrix dominates the oscillation of atmospheric neutrinos, the third the solar neutrino oscillation. The main unknown in this decomposition is the third mixing angle θ_{13}. At present, the upper limit for $\sin^2(\theta_{13})$ is 0.06 from the CHOOZ reactor experiment [147]. This limit is now supplemented by a three-flavour analysis of the SuperK atmospheric data, giving limits of $\sin^2(\theta_{13}) < 0.14$ and $\sin^2(\theta_{13}) < 0.27$ at 90 % confidence level for the normal and inverted mass hierarchy, respectively (see section 1.8). The CP violating phase $e^{i\delta}$ is currently completely unknown and the chances of measuring it will depend very much on the magnitude of θ_{13}. More detailed discussions of the effects of three-flavour mixing and its experimental signatures can be found in, for example, Refs. 148–151.

1.8 Discussion and outlook

Although neutrino oscillations are now a well established fact and the mass differences and mixing angles are already relatively well constrained, there are many remaining questions regarding the intrinsic properties of neutrinos.

Concerning neutrino oscillations, the third mixing angle and the CP violating phase remain the main unknowns. New reactor experiments with two detectors could possible observe the modulation of the $\overline{\nu}_e$ disappearance due to the θ_{13} angle. Another possibility is to observe the appearance of ν_e in a pure ν_μ beam. Currently, all results on neutrino oscillations for solar, atmospheric and reactor neutrinos are from disappearance experiments. The one exception is the neutral-current result of the SNO experiment which has measured the total solar-neutrino rate. However, also that result can not distinguish the weak eigenstates involved in the interactions. No experiment has as yet seen the appearance of the other neutrino states in oscillation.

Confirmation of the suggested oscillation channels can only be established by actually seeing the appearance of the other weak eigenstates due to oscillation. Such experiments are currently becoming operational at existing long-baseline neutrino beams (OPERA and MINOS). Other such experiments are being proposed using new neutrino beam concepts, like a muon storage ring or a beta-beam. In a muon storage ring [152], a beam of high-energy muons circulates inside a racetrack shaped ring. The decays of muons in the straight sections generates an intense neutrino beam. Such a storage ring is an ideal

source for appearance experiments as it produces only ν_μ and $\overline{\nu}_\mathrm{e}$ neutrinos (or the inverse) with well-known energy spectra and with energies above threshold for charged-current reactions of either ν_μ or ν_τ. The proposed beta-beam of radioactive nuclei [153] with its pure ν_e or $\overline{\nu}_\mathrm{e}$ flux is also a very clean neutrino source which makes detailed studies of neutrino oscillations possible.

The neutrino oscillation experiments have determined the two mass differences, but cannot determine the absolute mass scale. However, the lowest limit for any of the neutrino species is also a limit for the absolute mass scale. The current lowest limit is about 3 eV from the direct ν_e mass measurement. As the neutrino mass limits follow the same hierarchy in mass as the corresponding leptons, the most likely experiments to lower the absolute mass-scale limit are direct ν_e mass measurements. Currently a new tritium-decay experiment, called KATRIN, is being set up in Karlsruhe that will be able to measure down to $m_{\nu_\mathrm{e}} \leq 0.2\,\mathrm{eV}$ [154]. In the special case that neutrinos are Majorana particles (see below), the absolute mass could also be determined from the rate of neutrinoless double β-decay.

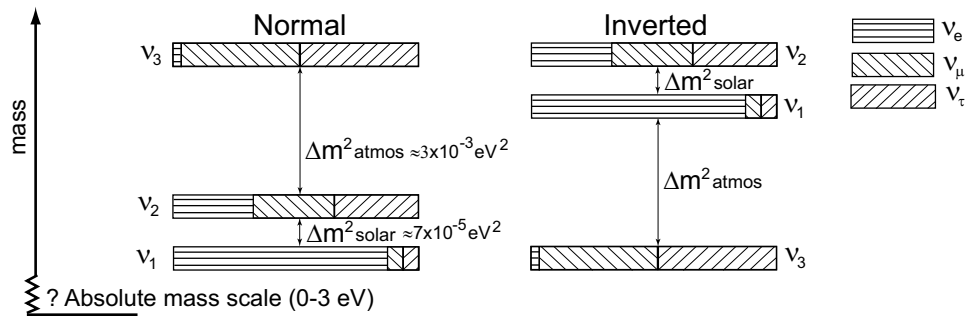

Figure 1.26: The two mass differences, measured for solar and atmospheric neutrinos, can be arranged in two different ways. Currently no experimental result can distinguish between the two. Also the absolute mass scale is currently unknown, although the direct ν_e mass measurements set an upper limit of about 3 eV.

The three neutrino masses can also be arranged in two different ways, called normal and inverted hierarchy, illustrated in Figure 1.26. Which particular hierarchy is right is yet unknown. If the absolute masses are close to the mass differences and the neutrino is a Majorana particle, neutrinoless double β-decay could determine the mass hierarchy. If, on the other hand, the absolute mass scale is high with respect to the larger Δm^2, the neutrino mass-eigenstates are almost degenerate and the hierarchy can only be established by observing the sub-dominant oscillation in very accurate oscillation experiments.

There are two ways (or a linear combination of both) in which neutrino masses can be introduced in the Lagrangian of the standard model, known as a Dirac or Majorana mass-term. In any case, because the neutrinos have mass, right-handed neutrinos exists as well. If the neutrino is a Dirac particle, the right-handed neutrino state is generated by a Lorentz transformation of the left-handed helicity state. If the neutrino is instead a Majorana particle, the right-handed state corresponds to the anti-neutrino. This coupling between helicity and particle or anti-particle state is only allowed for neutrinos because they carry no conserved quantities. If the neutrino is a Majorana particle, an emitted

neutrino can interact as an anti-neutrino with a probability given by its mass. In this case neutrinoless double β-decay becomes possible for some nuclei. The Feynman diagram for neutrinoless double β-decay is depicted in Figure 1.27. The rate of this process can then be used to measure the absolute mass of the neutrino (if all the nuclear matrix elements can be calculated [155]). On the other hand, if neutrinoless double β-decay is not observed and the absolute mass scale is larger than 1 eV, one can conclude that neutrinos are Dirac particles.

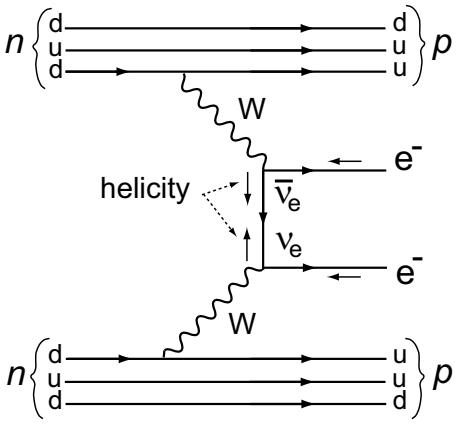

Figure 1.27: Feynman diagram of neutrinoless double β-decay. In this process a nucleus emits two electrons but no neutrinos when two neutrons change into two protons. The neutrino emitted in the first β-decay is absorbed as an anti-neutrino in the second β-decay, which is only possible if the neutrino is a Majorana particle and has non-zero mass such that its helicity, indicated by the small arrows, is not a conserved property.